
**Università degli Studi di Pisa**
**Dipartimento di Ingegneria dell'Energia e dei Sistemi**

Ph.D. course in Automation, Robotics and
Bioengineering – Course Cycle XXVI
SSD: ING-INF/06

Ph.D. Dissertation on

# New Methods in Cardiac Magnetic Resonance Imaging and Spectroscopy

Candidate student:
Nicola Martini

Supervisor:
Prof. Maria Filomena Santarelli

# Contents

# List of Figures

# List of Tables

# Abstract

Magnetic Resonance Imaging (MRI) and Spectroscopy (MRS) are non-invasive techniques that provide fundamental information for tissue characterization in normal and diseased myocardium. Indeed, quantitative MRI gives insight into different pathophysiological conditions of myocardial tissue, like inflammation, edema and fibrosis, while MRS allows the quantification of crucial compounds involved in myocardial energy metabolism, such as triglycerides (TGs) and creatine (CR).

The purpose of this thesis is to address several methodological challenges that have limited so far the application of these techniques in clinical settings, such as the low signal-to-noise ratio (SNR), the susceptibility to motion, the long scan times and the reproducibility of quantitative parameters.

To achieve this purpose, the use of large coil arrays for SNR enhancement in cardiac MRS was investigated and advanced motion compensation strategies were implemented to increase the reproducibility of metabolite quantification. Moreover, in order to assess the regional distribution of myocardial TGs and CR in short scan times, a fast spectroscopic imaging technique was proposed and

validated on healthy volunteers. Finally, a quantitative MRI method was implemented on a 3.0 Tesla MRI system for mapping T1 relaxation times in the human heart.

The results achieved by the methods proposed in this thesis may facilitate the use of cardiac MRI and MRS in clinical routine for an accurate characterization of myocardial tissue.

# Chapter 1

# Introduction

Magnetic Resonance Imaging (MRI) and Spectroscopy (MRS) are noninvasive techniques that provide complementary information for myocardial tissue characterization. MRI takes advantage of the different magnetic properties of water protons (relaxation times, proton density) for the generation of image contrast between tissues. On the other hand, MRS allows the detection and the quantification of other molecules, by exploiting the fact that protons of different compounds resonate at different frequencies and thus they can be discriminated in a MR spectrum.

In particular, proton MRS ($^1$H-MRS) allows the noninvasive detection *in vivo* of metabolites associated to cardiac diseases. Cardiac $^1$H-MRS studies [1,2] reported that a link between the accumulation of myocardial triglycerides (TGs) and cardiac dysfunction exists, and that a reduction of creatine (CR) can be observed in the failing heart [3].

However, several methodological challenges limited the reproducibility and the application of cardiac MRS in clinical settings.

Firstly, MRS signals are inherently characterized by low signal-to-noise ratios (SNRs) due to the low concentration of cardiac metabolites, which is several orders of magnitude lower than those of water protons. Also, a proper suppression of the water signal during acquisition [4] and/or post-processing [5] is necessary for an accurate quantification of the metabolite concentrations.

Secondly, cardiac and respiratory movements further reduce the SNR and degrade the quality of the acquired spectra, thus limiting the reproducibility of cardiac $^{1}$H-MRS experiments.

Furthermore, single-element receiver coils are traditionally used in cardiac MRS studies [1, 6]. Since these coils are characterized by a limited spatial coverage, the SNR of MRS signals can be affected by imperfect coil positioning over the chest of the patients. Coil repositioning has been reported in literature to reach sufficient SNR levels [6]. A possible solution would be the use of multi-element receiver coils, named *coil arrays*, which are routinely adopted in cardiac MRI for their increased spatial coverage.

Another main issue of cardiac proton spectroscopy concerns spatial information. Cardiac $^{1}$H-MRS studies reported in literature are based on single-voxel (SV) spectroscopy techniques [2, 6, 7]. Using these techniques, the signal is received from a relatively large single-volume of interest (VOI), which is typically placed in the interventricular septum to avoid the signal contamination from blood and pericardial fat. Since SV techniques are unable to measure heterogeneous distributions of metabolite content across the VOI, only

alterations with global effects on the heart can be studied. In order to study alterations distributed locally rather than diffusely, multi-voxel spectroscopic techniques should be adopted.

The most common multi-voxel spectroscopic technique is the Chemical Shift Imaging (CSI), which is based on the phase encoding concept used in MRI for spatial localization. Conventional CSI is the optimal technique in terms of sensitivity per unit time [8], but the extremely long acquisition times limited the application *in vivo*. Although several approaches have been proposed to accelerate CSI acquisitions, including k-space undersampling and volume pre-localization methods [9], CSI experiments still require too long scan times to obtain adequate spatial resolutions and field on views for cardiac $^{1}$H-MRS.

A fast alternative to CSI is the Echo Planar Spectroscopic Imaging (EPSI) technique, in which oscillating gradients during signal acquisition encode simultaneously the spatial and the spectral dimension [10]. EPSI data acquisition is then much faster than CSI, since one spatial dimension is encoded in a single-shot. However, EPSI studies reported in literature are limited to the human brain [11] or other non-moving organs [12].

Quantitative Magnetic Resonance Imaging (MRI) techniques can provide complementary information to MRS in the field of myocardial tissue characterization [13, 14].

The purpose of quantitative MRI is the measurement of magnetic properties of tissues, such as the relaxation times. Longitudinal relaxation time or spin-lattice relaxation time (T1) is the time constant that rules the exponential recovery of longitudinal magne-

tization equilibrium. Since T1 relaxation time depends on the chemical and physical environments of water protons [15], T1 values vary significantly among different tissues, but also among different physiopathological conditions in the same tissue, like infarction, edema and fibrosis.

Initial attempts to myocardial T1 quantification were limited to region of interest (ROI) analysis [16], rather than a pixel-by-pixel T1 estimation, i.e. T1 mapping. The first successful implementation of myocardial pixel-wise T1 mapping was based on the Modified Look-Locker Inversion Recovery (MOLLI) method [17], which allowed the acquisition of several images at different inversion times but in the same cardiac phase and in a single breath-hold, and thus to obtain T1 maps of the heart. The MOLLI approach inspired the development of several variants of the original method, based on either on inversion recovery [18] or saturation recovery sequences [19]. However, differences in T1 values obtained either from different protocols or from different regions of the myocardium have not been well investigated. Moreover, most of myocardial T1 mapping studies have been performed with 1.5 Tesla MRI systems, since several disadvantages at higher field strengths, like increased field inhomogeneities, longer T1 and power deposition, make T1 mapping more challenging.

The PhD project is focused on the development of new methods in Cardiac Magnetic Resonance Imaging and Spectroscopy for the noninvasive myocardial tissue characterization *in vivo*.

The purpose of the first part of the thesis, described in Chapter 2, was twofold: 1) to explore the use of multi-element coils, commonly used in MRI, for the SNR enhancement of cardiac $^{1}$H-MRS

signals; 2) to develop respiratory motion compensation strategies to increase the reproducibility of cardiac metabolite quantification in single-voxel $^{1}$H-MRS.

The objective of the second part of the thesis, described in Chapter 3, was the implementation of a fast spectroscopic imaging technique, based on the EPSI sequence, able to provide regional distribution of cardiac metabolites. This technique was tested on healthy volunteers and quantification results were compared with those obtained using single voxel spectroscopy.

The third part of thesis, described in Chapter 4, is focused on the development of a myocardial T1 mapping technique based on the MOLLI approach. Numerical simulations showed the influence of pulse sequence parameters on T1 estimation and *in vivo* results obtained with a 3.0 Tesla MRI system are presented.

# Chapter 2

# Cardiac Proton Spectroscopy using Large Coil Arrays

The first part of the PhD work was focused on the use of coil arrays for cardiac proton spectroscopy ($^1$H MRS). The respiratory navigator techniques was integrated into a single-voxel spectroscopy sequence for reducing respiratory motion effects. Different reconstruction techniques of ($^1$H MRS) from coil arrays were compared, and *in-vivo* results were obtained with 32- and 5-element coil arrays in healthy volunteers.

The results of this work have been published in the following article: K. Weiss, N. Martini, P. Boesiger, S. Kozerke. "Cardiac proton spectroscopy using large coil arrays", *NMR Biomed.* 2013 Mar; 26(3): 276-84 [20].

## 2.1 Cardiac Magnetic Resonance Spectroscopy

Magnetic resonance spectroscopy (MRS) can provide fundamental insights into the role of cardiac metabolism in normal and diseased hearts [21, 22]. Localized proton MRS ($^1$H-MRS) in particular has been demonstrated to be a valuable technique for the noninvasive measurement of human myocardial triglyceride (TG) and total creatine (CR) content [1, 3, 6, 23]. Recent studies based on $^1$H-MRS have highlighted correlations between lipid accumulation in the myocardium and reduced cardiac function, and they have revealed the role of steatosis in the pathogenesis of type 2 diabetes mellitus [1,2,7] Assessment of total CR content, which reflects the sum of creatine and its phosphorylated form phosphocreatine, has been reported and depletion in the failing heart demonstrated [3, 23].

Several technical and practical issues have, however, limited the widespread use of cardiac 1H MRS in clinical routine so far. Cardiac and respiratory motions degrade the spectral quality because of inhomogeneous B0 and B1 fields, outer voxel contamination and phase changes as a result of motion of the spins during localization gradients. Although electrocardiogram (ECG) triggering to end-systole is commonly used to synchronize volume selection and data acquisition with cardiac motion, several approaches have been proposed to compensate for respiratory motion. Triggering based on respiratory signals provided by air-pressure sensors has been shown to improve the quality of cardiac spectra [24]. Breath-holding has been used to assess myocardial TG content [25, 26]. However, re-

stricted breath-hold durations inherently limit the number of signal averages, and hence the sensitivity for the detection of myocardial CR. An alternative method used to synchronize the acquisition to end-respiration is based on navigator echoes to measure the position of the diaphragm [27, 28]. Navigator gating has been found to be a prerequisite for the reproducible assessment of myocardial TGs [6].

Other practical issues of cardiac MRS concern radiofrequency (RF) coil selection and coil placement for signal reception. Traditionally, single-element surface coils are positioned on the chest wall of the subject. However, the use of single-loop coils has drawbacks. The limited spatial coverage requires careful positioning of the coil as close as possible to the region of interest to maximize the signal-to-noise ratio (SNR). Coil repositioning is necessary in some cases to accurately place the coil center over the mitral valve level of the heart [6]. At the same time, single channel receive coils continue to be replaced by coil arrays on modern MR systems, providing larger spatial coverage and permitting accelerated acquisition using parallel imaging techniques. Coil arrays with 32 elements are becoming a standard for highly accelerated cardiovascular imaging [29, 30]. The large spatial coverage provided by these coil arrays renders coil repositioning during examinations unnecessary. Accordingly, it would be desirable to use large coil arrays for both imaging and spectroscopy of the heart, and thereby facilitate the integration of cardiac $^{1}$H MRS into clinical workflow.

## 2.2 Multichannel Magnetic Resonance Spectroscopy

The use of a set of receive coils, called *phased array* [31], is commonly adopted in MRI to increase spatial coverage and to accelerate the acquisition through parallel imaging techniques [32]. As magnetic resonance spectroscopy is characterized by low sensitivity, the use of phased arrays can be exploited to improve the signal-to-noise ratio (SNR). To this end, individual coil signals have to be properly combined taking into account coil sensitivity and noise to maximize the resulting SNR.

### 2.2.1 Signal modelling

The MRS signal acquired by a phased array can be modelled in time domain as follows:

$$\begin{aligned} x_m(n) = s_m \exp^{\iota\varphi_m} \widehat{x}(n) + \epsilon_m(n) = s_m \exp^{\iota\varphi_m} \\ \sum_{k=1}^{K} a_k \exp^{\iota\theta_k} \exp^{(-d_k+\iota 2\pi f_k)n\Delta t} + \epsilon_m(n) \\ \text{with } n = 0, 1, \ldots, N-1 \text{ and } k = 1, \ldots, K \end{aligned} \tag{2.1}$$

where $N$ is the number of samples, $M$ is the number of coils, $K$ is the number of metabolites, $\epsilon_m(n)$ is a complex Gaussian noise term. Each metabolite is modelled with a complex damped sinusoid with amplitude, phase, damping factor and resonance frequency denoted by $a_k$, $\theta_k$, $d_k$, and $f_k$ respectively.

The gain factor $s_m$ takes into account the amplitude variations due to the different sensitivity of each $m$ coil, while $\varphi_m$ is the phase

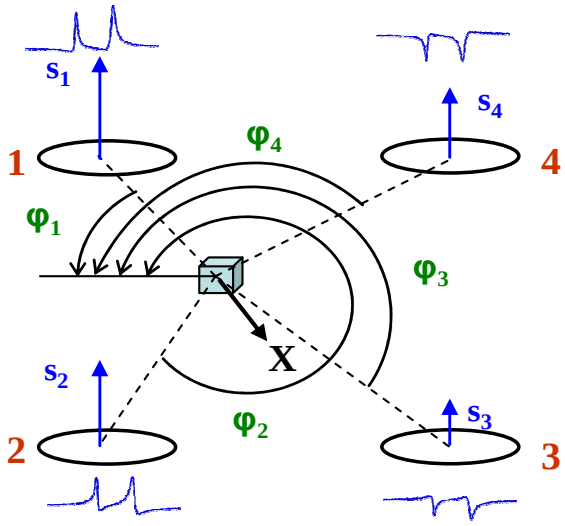


Figure 2.1: Model of the MRS signal acquired by a four-element phased array coil.

shift dependent on the receiver position.

To introduce in the model the effect of noise coupling between the receivers, correlated noise $\epsilon$ among coils is generated by mixing $M$ circular complex white noise sources, using a square $M \times M$ matrix with appropriate non-zero elements off the diagonal [33].

### 2.2.2 Coil combination

The optimization of the SNR in multichannel spectroscopy requires the proper combination of the individual signals. The combined signal optimized signal $x_c$ is given by the weighted summation of the individual signals $x_i$

$$x_c = \sum_{i=1}^{M} w_i x_i = \sum_{i=1}^{M} |w_i| \exp^{\iota\varphi_i} x_i \tag{2.2}$$

where $w_i$ are complex weighting factors with magnitude $|w_i|$ that explains the gain of the $i$-th coil, and angle $\varphi_i$ that reflects its phase shift.

In the following, three different coil combination strategies for multichannel cardiac $^1$H MR spectroscopy are presented.

### SNR weighting

In the first approach the amplitude of the coil weights are proportional to the SNR [34]. The SNR of every coil is calculated as the ratio of the signal amplitude and the standard deviation (SD) of the noise in the time domain. The phase and amplitude of the water-unsuppressed signals were estimated from the first points of the FID (Free Induction Decay); the SD of the background noise was estimated from the last points of the FID when the signal had already decayed.

The SNR and phase of every coil were used to estimate the complex weighting factors $w_i$. The coil signals were subsequently combined according to Equation 2.2.

### PCA combination

The second approach is based on principal component analysis (PCA) of the coil signals [35,36]. PCA is used to reduce the dimensionality of a problem by projection onto a subspace.

In the case of coil combination for single-voxel spectroscopy, the Hermitian matrix $Q$ was calculated according to:

$$Q = \sum t\widehat{S}(t)\widehat{S}(t)^H \tag{2.3}$$

where $\widehat{S}(t)$ contains the data from all $M$ coils for time point $t$ of the FID. PCA was used to perform a singular value decomposition of $Q$ such that:

$$Q = UFV^H \tag{2.4}$$

with $F$ containing the sorted eigenvalues as described in ref. [37] for coil array compression. The complex coil weights $w_i$ were approximated by the first column of $U$ and the signals were combined according to Equation 2.2.

Two different coil combination strategies based on the PCA approach were compared. PCA combination of water unsuppressed reference scans ($PCA_w$) and PCA combination of the mean signals of the water suppressed reference scans ($PCA_s$).

### Image-based combination

In this approach, complex coil weights were estimated from complex valued reference images that are usually acquired for the optimal of the acquisition volume. Typically, reference images were localized in short-axis (SA) and four-chamber view (4CH) to accurately place the single-voxel volume in the inter-ventricular septum.

All pixels within the region of the SV (red box in Figure 2.2) were averaged and normalized, leading directly to the complex coil weights $w_i$ which were used for coil combination according to Equation 2.2.

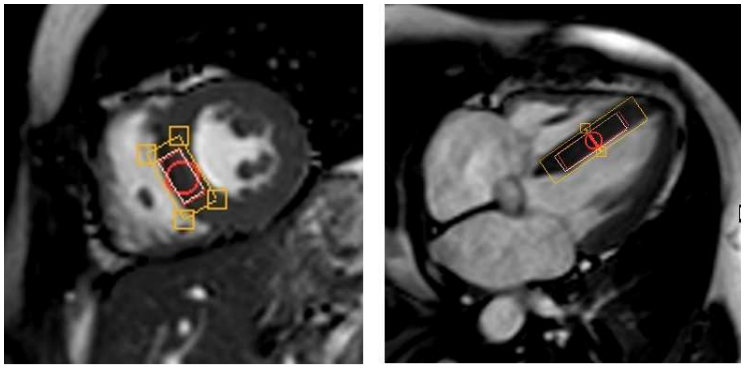

Figure 2.2: Single-voxel in short-axis (left) and four-chamber (right) view images.

### 2.2.3 Numerical simulations

Numerical simulations were carried out to investigate the noise dependence of the $PCA_s$, $PCA_w$ and $SNR_w$ coil combination methods. Water unsuppressed and water suppressed spectra including three lipid resonances with chemical shifts of 0.9, 1.3 and 2.1 ppm, the CR resonance at 3.01 ppm and the resonance of TMA at 3.2 ppm were simulated using parameters obtained from an *in vivo* scan. To simulate the 32-channel array, the simulated FIDs were split into 32 channels using complex coil weighting factors $w_i$ estimated from an *in vivo* scan using the $SNR_w$ approach. Random noise was added to the individual coil signals to provide SNR values of the main TG peak at 1.3 ppm of 3, 4, 5, 6, 8, 13, 23, 38 and 50 in the coil-combined water suppressed signals and associated SNR values of 100, 150, 200, 250, 300, 500, 900, 1500 and 2000 of the water peak in the coil-combined water-unsuppressed signals. To optimize the $PCA_s$ coil combination strategy, the Hermitian matrix $Q$ in Equa-

tion 2.3 was calculated from a filtered subset of the FIDs which were filtered using a matched filter and cropped to an acquisition time of $T_{FID} = 2\,T_2^*$ according to ref. [38], where $T_2^*$ is the exponential decay time estimated from the FID of the coil with the highest signal.

Complex coil weighting factors $w_i$ were estimated using the $\mathrm{PCA_s}$, $\mathrm{PCA_w}$ and $\mathrm{SNR_w}$ approaches and the signals were subsequently combined according to Equation 2.2. As a reference standard, the simulated signals were additionally combined using the known correct complex coil weights $w_i$ used for simulating the signals of the individual coils. All simulations were repeated 100 times.

## 2.3 Respiratory motion compensation

ECG triggering, i.e. triggering the acquisition in a fixed phase of cardiac cycle using the ECG signal, effectively removes the effects of cardiac motion. However, with breathing the heart is subject to substantial displacement, especially in the superior-inferior (SI) direction.

Respiratory motion causes several negative effects on the reliability of cardiac $^1$H MR spectroscopy. Firstly, the acquisition volume can be contaminated by the blood pool, yielding inaccurate quantification of myocardial metabolites. Secondly, the displacement of the acquisition volume often impairs the shimming procedure, leading to spectral line broadening. Moreover, phase differences between individual scans increases with motion, thus degrading the overall SNR.

In this study respiratory motion compensation was performed

using two complementary techniques. During acquisition, the *respiratory navigator* was used to collect $^{1}$H-MRS data in the same phase of the breathing cycle. In post-processing, *constructive averaging* was used to compensate residual respiratory motion.

### 2.3.1 Respiratory Navigator

Respiratory navigator (RNAV) collects data of a circular column of spins in the superiorinferior (SI) direction through the interface between the liver and the lung. The position of the diaphragm along the SI direction is quantified in real-time. During the calibration phase a number of RNAVs are sequentially acquired to estimate the excursion of the diaphragm in the breathing cycle, as shown in Figure 2.3 (a).

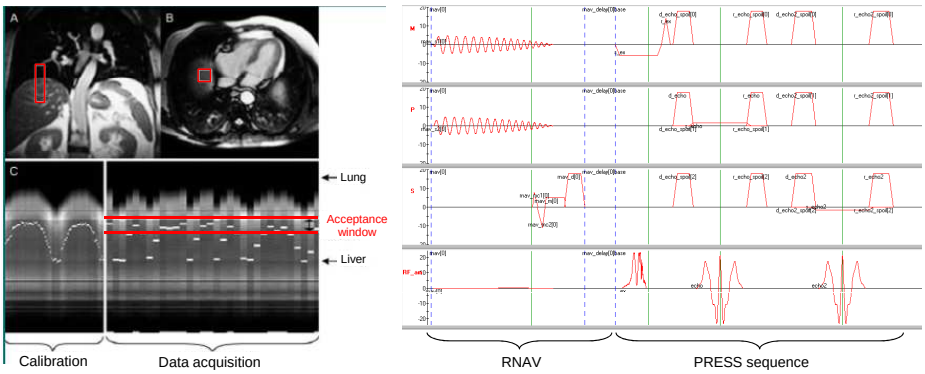


Figure 2.3: (a) Position of the pencil beam navigator (adapted from [6]). (b) Respiratory navigator pulse sequence.

For data acquisition, there are two main RNAV strategies: *triggering* and *gating*. With triggering the position of the diaphragm is

continuously monitored with RNAVs until it reaches the expiration level and then the acquisition starts. In gating, the edges in mm of the expiration phase are estimated during the calibration phase, thus defining the acceptance window of Figure 2.3 (a). Then, the RNAV is performed just before each acquisition and data are accepted or discarded whether the RNAV is within or outside the acceptance window respectively.

Respiratory navigator was integrated in point-resolved spectroscopy (PRESS) sequence for single-voxel $^{1}$H-MR spectroscopy. 2D pencil beam excitation was obtained using a spiral k-space trajectory as shown in Figure 2.3 (b). The RNAV was also inserted into the preparation phases commonly used in spectroscopy as a part of the prescan: F0 determination, shimming and automatic water suppression optimization (AWSO). Pulse sequence development was performed using the Pulse Programming Environment for the Philips Achieva MRI scanner (PARADISE version 2.6.3). Figure 2.4 shows the modified user interface of the MRI system, where RNAV parameters were enable in the PRESS sequence and in its preparation phases (F0 determination, shimming and AWSO).

### 2.3.2 Constructive Averaging

A common method to increase the SNR in magnetic resonance spectroscopy experiments is the averaging of $N$ acquisitions which, in case of uncorrelated noise, leads to a theoretical $\sqrt{N}$-fold SNR gain. However, motion in the presence of field gradients (used for PRESS localization) changes the phase of the echo signal, resulting in destructive interference when consecutive signals are averaged [39].

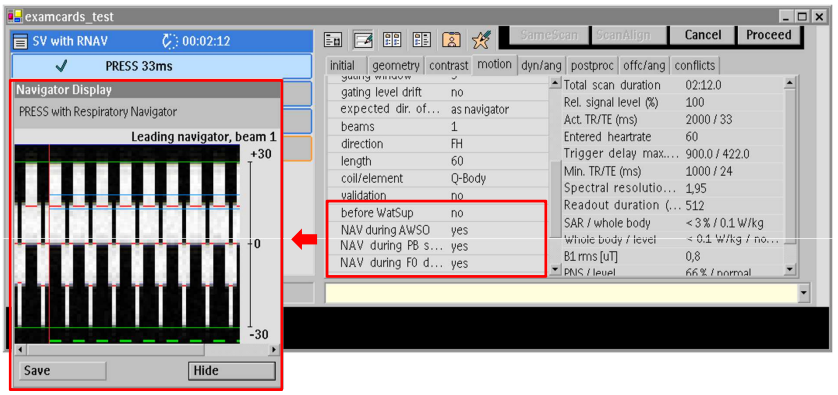


Figure 2.4: MRI system User interface with the integration of the respiratory navigator in the PRESS sequence.

The SNR loss is proportional to the phase dispersion of the signal due to motion.

It has been shown [39] that in case of uniform distribution of the phase over the interval $[\Phi_1, \Phi_2]$, the SNR loss proportional to the standard deviation SD of the phase variation:

$$\mathrm{SNR}_{\mathrm{loss}} = \mathrm{sinc}\left(\Phi_p/\pi\right) = \mathrm{sinc}\left(\sigma_\phi\sqrt{3}/\pi\right) \tag{2.5}$$

where $\Phi_p = \left(\Phi_1 - \Phi_2\right)/2$ is half of the range of the phase variation and $\sigma_\phi$ is the SD of the phase variation.

The *constructive averaging* method is based on the zero-order phase correction of each individual spectrum before averaging. The phase correction of the entire spectrum is performed after the estimation the phase of a reference peak, i.e. a peak in the spectrum with sufficient SNR. Theoretically, if the phase of the reference peak is correctly estimated, the SNR gain after constructive averaging is given by the reciprocal of 2.5.

## 2.3 Respiratory motion compensation

In this work, a constructive averaging procedure was implemented as final step of the workflow of the reconstruction of multichannel cardiac $^1$H-MRS signals. The chosen reference peak was the water peak in water-unsuppressed spectra and the triglyceride peak, located at 1.3 ppm, in water-suppressed spectra. To get a more reliable estimation of the phase and to avoid false artifacts peaks, the phase was computed by averaging $M = \sqrt{(N)}$ samples around the triglyceride peak [39], where $N$ is the total number of acquisition.

Figure 2.5 shows an example of constructive averaging applied to $N = 128$ free-breathing cardiac $^1$H-MRS acquisitions. The large phase variation among individual spectral is corrected using the triglyceride peak as reference, providing an averaged spectrum with a significant SNR improvement, where even the creatine peak is well detectable as shown in fig. 2.5 c.

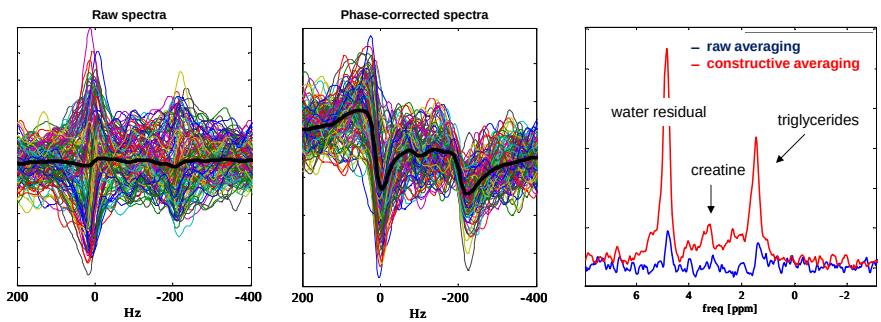


(a) (b) (c)

Figure 2.5: The large phase variation among individual spectral shown in a) is corrected in b) using the triglyceride peak as reference. Comparison between raw averaging and constructive averaging is shown in c).

## 2.4 Results

### 2.4.1 Experimental protocol

#### *In vivo* experiments

A short-TE (33 ms) navigator-gated point-resolved spectroscopy sequence (PRESS) [40] was used for single-voxel (SV) localization in the interventricular septum to avoid epicardial fat contamination. Pencil-beam navigator echoes were implemented for respiratory motion compensation [28]. Prior to data acquisition, iterative shimming was performed during a breath-hold using a voxel slightly larger than the SV. Navigator triggering was employed for water suppression optimization. The PRESS sequence was ECG triggered to the end-systolic phase, the minimum TR was set to 2000 ms and voxel dimensions were 10mm×20mm×40mm, resulting in an 8-mL volume. Water suppression was implemented using two frequency-selective RF pulses, each followed by a gradient spoiler; 1024 complex data points were collected with a spectral width of 2000Hz.

In vivo experiments were performed using a 1.5-T Philips Achieva system (Philips Healthcare, Best, the Netherlands) on a total of 15 volunteers who gave their written informed consent before participating in the study. Cine images in four-chamber (4CH) and short-axis (SA) views were acquired to accurately place the SV volume in the septum and to determine the trigger delay of the end-systolic phase. A balanced steadystate free precession sequence was used with the following parameters: TR = 3 ms; TE = 1.5 ms; flip angle, 60° spatial resolution, 2mm×2mm; slice thickness, 8 mm; 40 heart phases. Data were collected during free breathing using navigator gating in

end-expiration to plan the SV volume.

Two different protocols were used for the $^{1}$H MRS acquisitions. For the comparison of the 5- and 32-element cardiac coil arrays, experiments were performed on 11 volunteers (seven men, four women; mean age ± standard deviation (SD), 33±11 years; range, 20-54 years; mean body mass index±SD, 23±3kg/m2; range, 17-27 kg/m$^2$). In every acquisition, eight water-unsuppressed scans and 128 water-suppressed scans were acquired, resulting in an overall scan time of 11 min 20 s with a gating efficiency of about 40%. Both the 5- and 32-element cardiac coil arrays were used consecutively for signal reception in the same session, changing the order of both coils for every other volunteer.

To test reproducibility for each coil array, experiments were performed on four volunteers (two men, two women; mean age SD, 30±12 years; range, 21-47 years; mean body mass index SD, 24±2 kg/m2; range, 21-25 kg/m2). In every acquisition, eight water unsuppressed scans and 64 water-suppressed scans were acquired, resulting in an overall scan time of 6 min with a gating efficiency of about 40%. The volunteers were taken out of the scanner and were repositioned in between two subsequent scans using either the 5- or 32-element cardiac coil array for signal reception. The measurement was repeated using the other coil array for signal reception on the same volunteer in a second session. The time between the two sessions was approximately 1 week. Each session, including subject preparation, acquisition of MRI cine images and acquisition of MRS data, took approximately 1 h in total.

### MRS data processing

For each dataset, offline reconstruction of multichannel MRS data was performed using Matlab (The Mathworks, Natick, MA, USA). Data reconstruction steps are listed in Fig. 2.6. Noise covariance matrices were estimated from a separate noise scan and were used to decorrelate the coil channels before coil combination. This step has been shown to be a prerequisite for the optimal combination of spectra from receive coil arrays at low SNRs [33, 36].

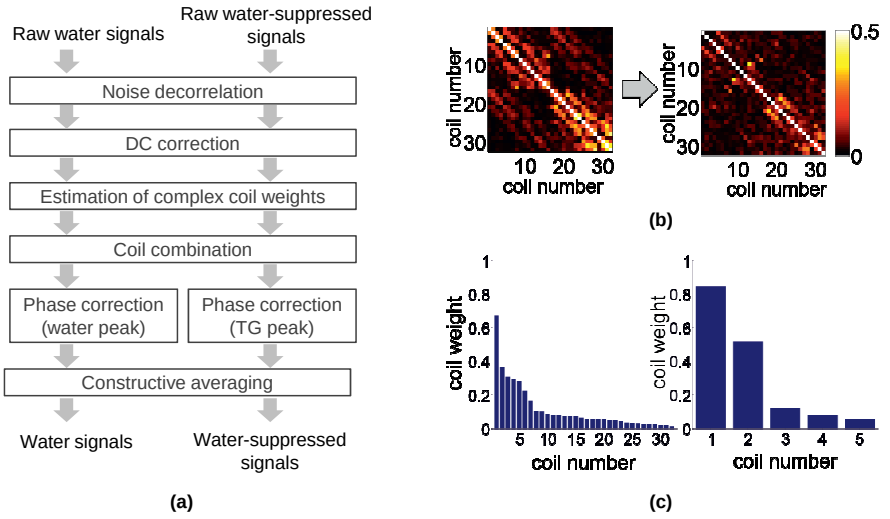


Figure 2.6: (a) Overview of the reconstruction steps of multichannel single-voxel data. (b) Noise correlation matrix of the 32-element coil signals before and after noise decorrelation. (c) Coil element weights for the 32-element and 5-element coil arrays are given as a function of the coil element number.

For subsequent coil combination, four strategies to estimate complex coil weights $w_i$ were compared (see section 2.2.2): SNR weight-

ing ($SNR_w$), PCA combination of water unsuppressed reference scans ($PCA_w$), PCA combination of the mean signals of the water suppressed reference scans ($PCA_s$) and image-based combination from from cine images in SA and 4CH orientations.

### Data analysis

Water-unsuppressed and water-suppressed spectra were fitted in the time domain using the AMARES function of the Java-based MR user interface software (jMRUI version 3.0) [41]. The full width at half-maximum (FWHM) of the water peak in water unsuppressed spectra was calculated. Three lipid resonances with chemical shifts of 0.9, 1.3 and 2.1 ppm, the CR resonance at 3.01 ppm and the resonance of the trimethylammonium (TMA) compound at 3.2 ppm were fitted in water-suppressed spectra. The sum of the amplitudes of the TG resonances at 0.9 and 1.3 ppm and the resonance of CR were divided by the amplitude of the water peak and multiplied by 100 to yield the percentage of myocardial TG and CR content [6]. Correction for longitudinal and transverse relaxation was applied using $T_1 = 1100$ ms and $T_2 = 40$ ms for myocardial water [15], $T_1 = 280$ ms and $T_2 = 86$ ms for TG estimated in skeletal muscle [42–44], and $T_1 = 1500$ ms and $T_2 = 135$ ms for myocardial CR [23, 42].

The SNR of the signals after coil combination was calculated from time domain amplitudes of the fitted water and main TG signals at 1.3 ppm and the SD of the last 128 points of the FID. To test differences between the individual measurements obtained with the 5- and 32-element coil arrays and the different coil combination

strategies, a two-tailed paired t-test was used. For comparison of the quantification results of TG content using the 5- and 32-channel coil arrays, intraclass correlation coefficients were calculated using a mixed effect analysis of variance. A level of $p<0.05$ was considered to be statistically significant.

### 2.4.2 Simulation results

Figure 2.7 shows the results of the numerical simulations. The signals were reconstructed with the $PCA_s$, $PCA_w$ and $SNR_w$ combination strategies and, after fitting in time domain, SNR values were calculated. SNR values in Fig. 2.7 are plotted against the reference SNR values for coil combination using the known weights $w_i$.

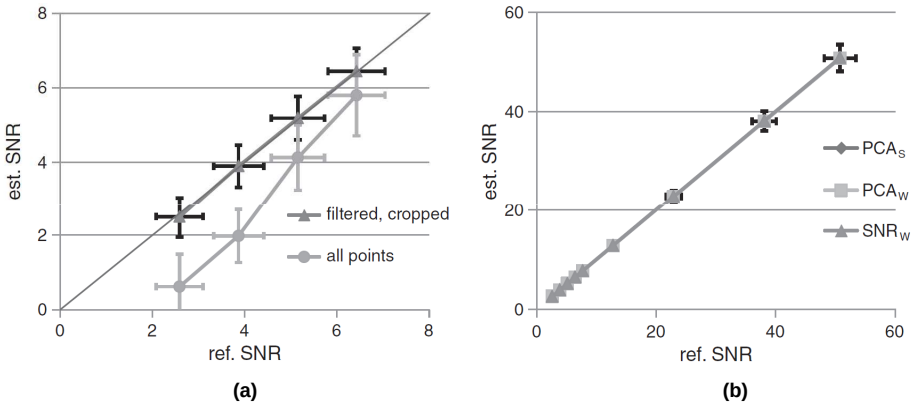


Figure 2.7: (a) Estimated SNR after coil combination using $PCA_s$ employing a filtered subset and all points of the FIDs to estimate the complex coil weights $w_i$. (b) Comparison of the $PCA_s$, $PCA_w$ and $SNR_w$ combination approaches.

For low SNR signals (SNR<10), the results of the numerical sim-

ulations revealed significant differences in the SNR after coil combination using the $PCA_s$ approach. However, no significant differences were found when only filtered subsets of the FIDs were used to calculate the complex coil weights $w_i$ employing the $PCA_s$ approach. Differences in the resulting SNR when the full FIDs or filtered subsets of the FIDs were used are shown in Figure 2.7a. However, no significant differences were found for high SNR values (SNR>10). Figure 2.7b compares the SNR of the three different coil combination strategies ($PCA_s$, $PCA_w$, $SNR_w$) relative to the SNR of the coil combination using known complex coil weights. No significant differences were found between the combination strategies.

### 2.4.3 *In vivo* results

Figure 2.8 shows representative spectra acquired with both coil arrays in three different volunteers.

Spectra obtained with the 32- and 5-channel coil arrays were found to agree well. In all spectra, the TG resonance at 1.3 ppm, the CR resonance at 3.01ppm and the resonance of TMA at 3.2 ppm were clearly visible. Spectral quality and sensitivity were found to be comparable for both coils.

*In vivo* spectra obtained with the 32- and 5-channel arrays for the four coil combination strategies are shown in Fig. 2.9. In all spectra, the resonances of TG, CR and TMA are well defined. Spectral quality and sensitivity appear to be similar in the spectra of the investigated coil combination strategies.

A quantitative estimation of the resulting SNRs using the $PCA_w$, $PCA_s$ and $SNR_w$ approaches for coil combination and the two coil

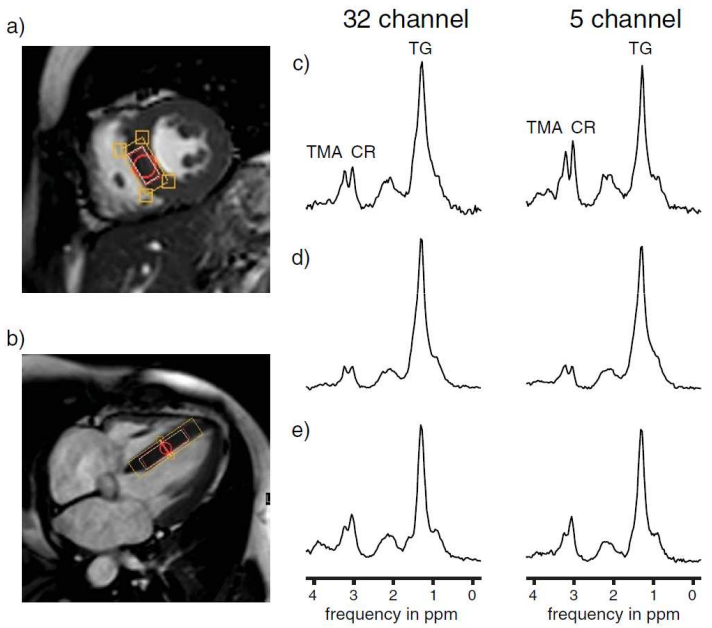


Figure 2.8: Position of the point-resolved spectroscopy (PRESS) voxel (inner box) and the shimming volume (outer box) in short-axis view (a) and four chamber orientation (b). (c-e) Spectra from three different volunteers acquired with the 32- and 5-channel coil arrays showing the resonances of myocardial trimethylammonium (TMA) compound, total creatine (CR) and triglycerides (TG).

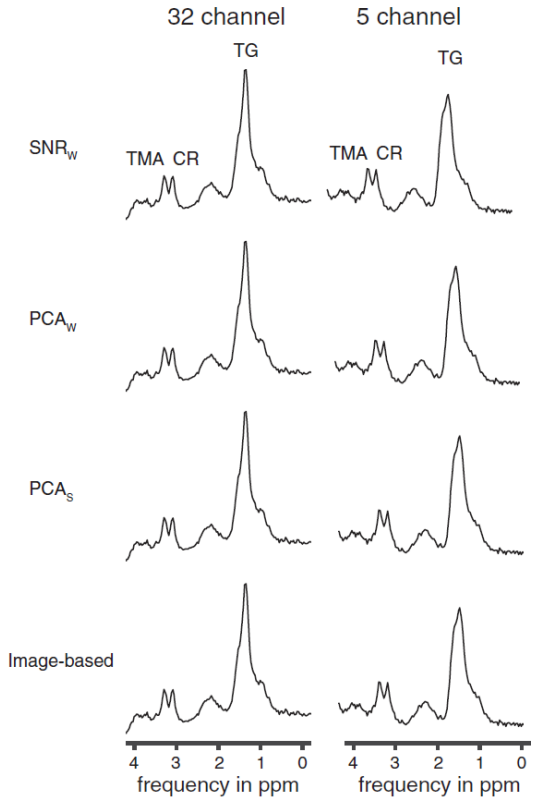


Figure 2.9: Spectra of one healthy volunteer. The signals of the individual coil elements were combined using $SNR_w$, $PCA_w$, $PCA_s$ and the image-based approach.

Table 2.1: Comparison of signal-to-noise ratio (SNR) performance of the different coil combination strategies using 5- and 32- channel coil array data. SNR was determined using the water and triglyceride (TG) peaks. For the $PCA_s$ approach, only the SNR of the TG peak was estimated, as no water reference is available for this method. All values are reported as the mean ± standard deviation.

| Reference | Coil | $SNR_w$ | $PCA_w$ | $PCA_s$ |
|---|---|---|---|---|
| Water | 5 | 2181±1067 | 2180±1067 | - |
| | 32 | 2698±1392 | 2700±1379 | |
| TG | 5 | 47.3±33.5 | 47.2±33.5 | 47.4±33.7 |
| | 32 | 53.8±33.9 | 54.0±33.9 | 54.1±33.8 |

arrays is given in Table 2.1. Differences between the mean values of the SNR for the combination approaches were found to be small for both coils, and not significantly different. SNR values obtained with the 32-element coil were 24% higher than those obtained with the 5-element coil array, on average (Table 2.1), although the differences did not reach statistical significance. SNR variations between subjects were found to be large, as reflected by the large SDs (Table 2.1).

Figure 2.10 shows the comparison between the complex coil weights $w_i$ estimated from water unsuppressed spectra using the $SNR_w$ approach and from images in SA and 4CH view orientations. For both coils, combination weights estimated from spectroscopic ($SNR_w$) and imaging data were found to be highly correlated.

Mean values of the FWHM of the water peak across all subjects

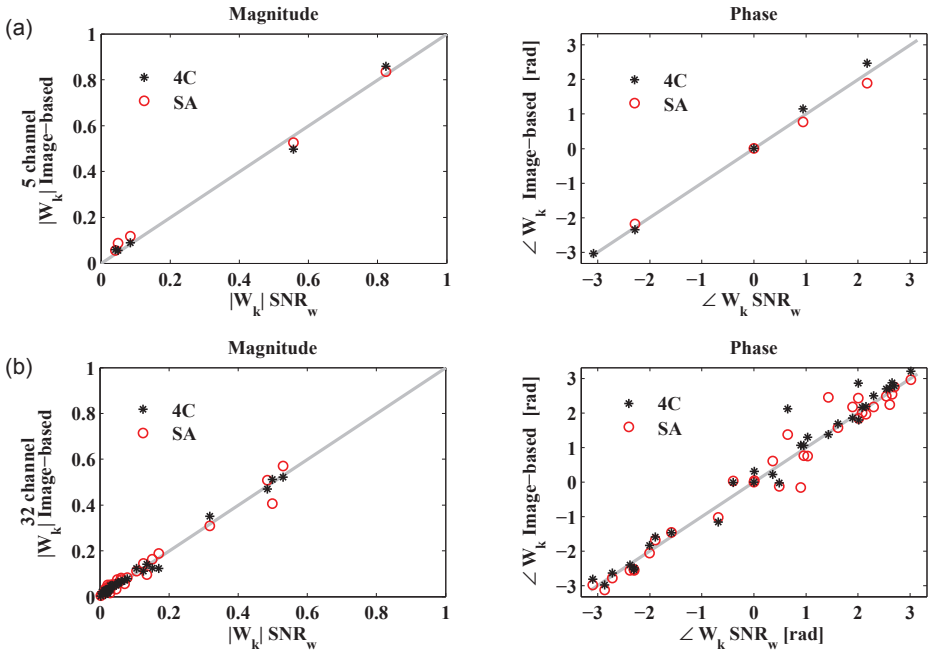


Figure 2.10: Comparison of complex coil weighting factors estimated using the signal-to-noise ratio (SNR) weighting ($SNR_w$) approach and the image-based approach for the 5-channel (a) and 32-channel (b) coil arrays. Angles reflect phase differences with respect to the coil element with maximum SNR. The line of identity is shown in gray.

Table 2.2: Full width at half-maximum (FWHM) of the water line, myocardial triglyceride (TG) and total creatine (CR) content estimated from 5- and 32-coil array data.d. All values are reported as the mean ± standard deviation.

| Coil | FWHM water | TG (%) | CR (%) |
|---|---|---|---|
| 5 | 8.6±1.5 | 0.45±0.17 | 0.05±0.01 |
| 32 | 9.8±2.0 | 0.44±0.19 | 0.05±0.02 |

and estimated values for myocardial TG and CR content after correction for $T_1$ and $T_2$ relaxation are shown in Table 2.2.

A close agreement is seen between the mean values across subjects obtained with the two coil arrays. In particular, the percentage of TG content was very consistent between the coil arrays, showing an intraclass correlation coefficient of 0.76 ($p<0.003$). No significant differences in the CR and TG contents between the two coil arrays were detected.

The test-retest reliability measurements on four healthy volunteers ($n = 4$) showed a higher SNR for the 32-channel array relative to the 5-channel array in both measurements (Fig. 2.11a).

However, no significant differences were found for estimated myocardial TG and CR content, either between two subsequent measurements with the same coil array or between the two coil arrays (Fig. 2.11b). Differences between coil combination approaches ($PCA_s$, $PCA_w$, $SNR_w$) were statistically nonsignificant.

For the 5-element coil, the two elements with the highest signal provided 99% of the SNR (Fig. 2.12a). For the 32-element coil, 16

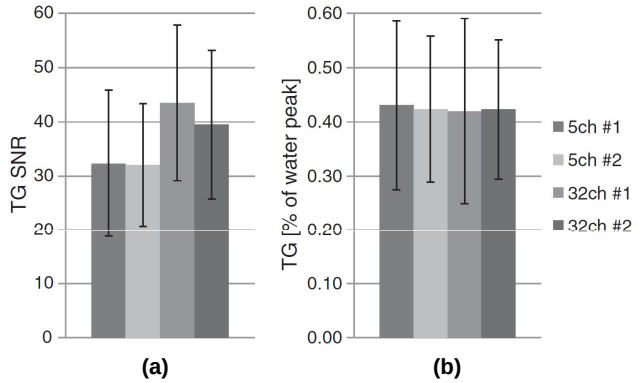


Figure 2.11: (a) Signal-to-noise ratio (SNR) of the main triglyceride (TG) peak at 1.3 ppm of the 5- and 32-channel coil arrays in the reproducibility experiments on four healthy volunteers. (b) Estimated myocardial TG content of the repeated measurements with both coil arrays given as a percentage of the water reference.

elements with the highest signals provided 99% of the SNR (Fig. 2.12b).

## 2.5 Discussion

The feasibility of $^{1}$H cardiac spectroscopy using large coil arrays has been demonstrated on healthy volunteers. The performance of a 32-channel coil array was assessed relative to a 5-channel array in the same scanning session. In all volunteers and with both coil arrays, spectral quality allowed for the estimation of CR and TG contents. The TG content showed a high correlation for both coil arrays, and no statistically significant variation of the estimated CR and TG contents was found between data obtained with the different arrays.

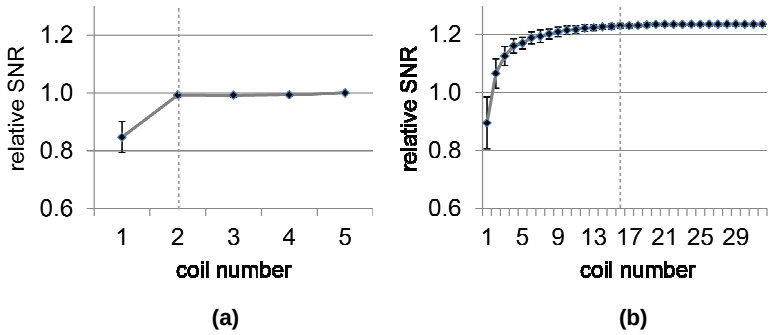


Figure 2.12: Relative signal-to-noise ratio (SNR) depending on the number of coils used for the reconstruction of the 5-channel (a) and 32-channel (b) coil array data. The data presented are the mean over all 11 volunteers reconstructed using the water-unsuppressed principal component analysis ($PCA_w$) approach.

Furthermore, estimated values for myocardial CR and TG contents are in good agreement with the values reported previously [6].

Four different strategies for coil combination were implemented and compared in terms of SNR performance using numerical simulations and *in vivo* measurements. The test-retest reliability of the measurements was evaluated on four healthy volunteers using both coil arrays and the presented coil combination strategies. No significant differences were found. Hence, the reproducibility of navigator-gated and cardiac-triggered SV spectroscopy reported previously [6] was confirmed. All coil combination approaches showed comparable SNR values and quality in the resulting spectra. However, the numerical simulations revealed a dependence of the $PCA_s$ approach on the number of points of the FIDs used to estimate the complex coil weights for low SNR (SNR$<$10). When a large number of points

of low SNR FIDs are used, the PCA is dominated by noise and the $PCA_s$ coil combination approach may fail, as shown in Fig. 2.7a. For low SNR data, it is beneficial to restrict the PCA to a small number of points at the beginning of the FIDs, where the signal is still high, before it decays into the noise level. To address this issue, a matched filter was applied and only a subset of the points of the FIDs [38] was used to estimate the complex coil weights $w_i$. Given these considerations, the numerical simulations did not reveal significant differences between the $PCA_s$, $PCA_w$ and $SNR_w$ approaches (Fig. 2.7b). In general, spectral quantification of TG becomes unreliable at SNRs below 10 and CR resonances approach noise level.

The investigated coil combination strategies differ in the amount of information required to estimate the complex coil weights $w_i$. Both the $SNR_w$ and $PCA_w$ approaches are based on water unsuppressed reference scans, which need to be acquired in addition. The $PCA_s$ approach, estimating the complex coil weights $w_i$ from the water-suppressed data, does not require additional data. Likewise, image-based coil weight estimation utilizes cine images, and hence makes use of survey images acquired in any case for SV planning purposes. Both $PCA_s$ and the image-based coil combination allow a shortening of the examination time if alternative quantification approaches are applied [45], and water reference data are not required as internal reference. However, for the estimation of the complex coil weights $w_i$ from images, the exact position of SV needs to be known and translated into the orientation of the image itself, adding some complexity to the reconstruction process when compared with the $PCA_s$ approach. Furthermore, the images need to be exported as complex data for every coil element, which is usually not part of

standard imaging workflow.

On average, the mean SNR of the 32-element array was about 24% higher (Table 2.1) than that of the 5-element coil. However, no statistically significant difference was found. This is related to the fact that a high variation of SNR between volunteers was detected, which led to large SDs of the mean SNR values. Parts of this large variation may be explained by variations in the cardiac trigger delay of the PRESS sequence as reported in [46].

In SV coil combination methods, only spectral correlations can be utilized, as demonstrated with the $PCA_w$ and $PCA_s$ combination strategies. In contrast, multivoxel techniques can take advantage of the spatial variation of coil sensitivities for optimal signal combination. To this end, the presented coil combination approaches can be applied on a voxel-by-voxel basis for spectroscopic imaging data.

Figure 2.13 shows the SNR after coil combination as a function of the size of the area of interest of a spectroscopic imaging scan using the 32-channel coil array. Three approaches were used for coil combination; voxel-wise $SNR_w$ and $PCA_w$ of a spectroscopic imaging scan [47] and, to simulate an SV, the $PCA_w$ coil combination after summing over all voxels in the area of interest. Voxel-wise $SNR_w$ and $PCA_w$ coil combinations showed similar performance. For a small number of voxels, the difference between the voxel-wise coil combination and the combination after averaging over all voxels, mimicking an SV, was found to be small. In the case of a single spatial point, all methods will give the same results. However, losses caused by spatial phase variations cannot be recovered in SV acquisitions and, accordingly, extended single volumes may compromise the optimal coil combination, as can be seen in Fig. 2.13. For typical SV sizes as

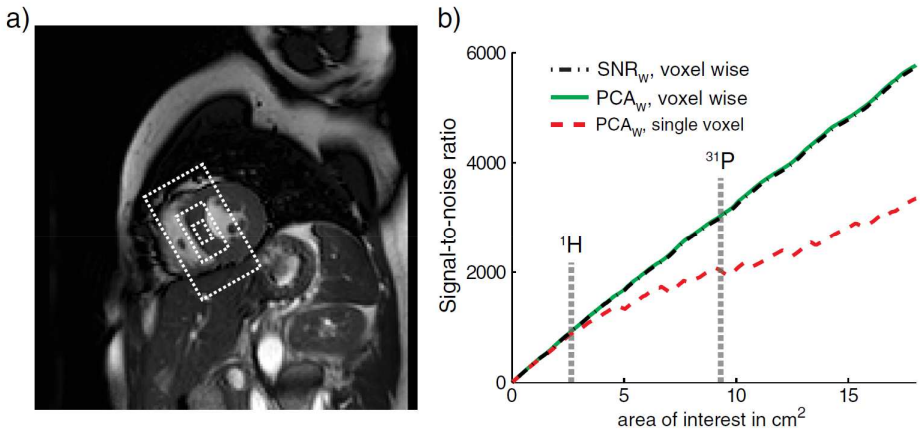


Figure 2.13: Signal-to-noise ratio (SNR) of the 32-channel coil array data as a function of the size of the area of interest in a spectroscopic imaging experiment. The two-dimensional spectroscopic imaging data were acquired using an echo planar spectroscopic imaging sequence with a 3mm × 3mm × 15mm resolution [47]. (a) Short-axis view image illustrating the different sizes of the areas of interest. (b) SNR for voxel-wise coil combination using the SNR weighting ($SNR_w$, voxel wise) and water-unsuppressed principal component analysis ($PCA_w$, voxel wise) approaches, and for coil combination after summing over all pixels in the area of interest using the $PCA_w$ approach, mimicking a single voxel ($PCA_w$, single voxel). Typical voxel sizes for $^{1}H$ and $^{31}P$ spectroscopy are indicated by the vertical broken lines.

used for $^{1}$H-MRS, losses caused by spatially varying coil phases are minimal and may be neglected. However, for MRS of less sensitive nuclei, such as phosphorus, larger voxels are used and losses caused by spatial variations of coil phases may become more prominent.

Given the availability of large coil arrays in cardiovascular imaging today, these results of this work will contribute towards the integration of cardiac spectroscopy into clinical protocols. In addition to an advantage in SNR performance, large coil arrays also provide sufficient coverage, and hence render coil repositioning during examinations unnecessary.

# Chapter 3

# Echo-planar spectroscopic imaging of the heart

The objective of this part of the PhD work was the development of an Echo-Planar Spectroscopic Imaging (EPSI) technique for the regional quantification of myocardial triglycerides (TG) and creatine (CR) content *in vivo*. Suitable reconstruction methods of cardiac EPSI data were implemented to perform coil combination, artifact ghost correction and B0 correction. The EPSI technique was tested on healthy volunteers and compared to single voxel spectroscopy.

The results of this work have been published in the following article: K. Weiss, N. Martini, P. Boesiger, S. Kozerke. "Metabolic MR imaging of regional triglyceride and creatine content in the human heart". *Magn Reson Med.* 2012 Dec; 68(6): 1696-704 [47].

## 3.1 Introduction

Single voxel proton magnetic resonance has been shown to be a promising tool for assessing total creatine (CR) and triglyceride (TG) content in the myocardial muscle in humans [1, 3, 48]. The specificity of *in vivo* proton magnetic resonance spectroscopy to probe myocardial TGs in humans has recently been validated [49].

Myocardial TGs,a cellular storage form of fatty acids, are indirectly connected to myocardial energy metabolism [50]. Therefore, one focus of interest is the correlation between myocardial TG content and cardiac dysfunction [2]. Total CR, which reflects the sum of CR and its phosphorylated form phosphocreatine, gives insight into the myocardial CR kinase reaction [3]. Being the primary energy reserve in myocardial tissues during periods of ischemia, hypoxia, and stress [22, 51], the CR kinase reaction reversibly transfers high-energy phosphate between phosphocreatine and adenosine triphosphate. It has been found that total CR content is depleted in the failing heart [3, 23].

Although spectral information from a single volume is sufficient when alterations with global effects on the heart are studied, a demand for higher and flexible spatial resolution exists when probing local changes, like in ischemic heart disease [22, 52].

Spectroscopic imaging has been used previously for studying high energy phosphates using $^{31}$P spectroscopy in humans *in vivo* [53–55]. Because of the low sensitivity of this nucleus, spatial resolution is very limited and methods utilizing protons as a signal source are preferred. To this end, implementation of $^{1}$H spectroscopic imaging of the heart can give insight into regional differences of total

CR and TG content and hence potentially allows for detection of heterogeneous myocardial pathologies.

Technically, $^{1}$H spectroscopic imaging of the heart is challenging. Results of earlier attempts of spectroscopic imaging of myocardial TG content were found to be dominated by epicardial lipids [48]. Parts of the problem have been associated with motion sensitivity and the long scan times. To compensate for cardiac and respiratory motion, navigator-based dual triggering has been proposed [27, 28], which has been found to be a prerequisite for reproducible proton spectroscopy of the heart [1, 6]. However, long scan times of conventional phase encoded chemical shift imaging techniques make cardiac spectroscopic imaging with sufficient resolution and size of the field of view not feasible. Therefore, fast spectroscopic imaging techniques trading signal-to-noise ratio per unit time and effective scan time are needed [8].

The objective of this work was to implement and optimize an echo-planar spectroscopic imaging (EPSI) technique [10, 56], which permits mapping of spatial distribution of TG and total CR content of the *in vivo* heart during free breathing acquisitions.

## 3.2 EPSI sequence

A local-look navigator gated spin-echo EPSI (Fig. 3.1) sequence was implemented on a 1.5 T Philips Achieva system (Philips Healthcare, Best, The Netherlands).

For all experiments, an equatorial slice in short axis view was acquired (Fig. 3.2 a,b). To avoid signal contamination from tissue

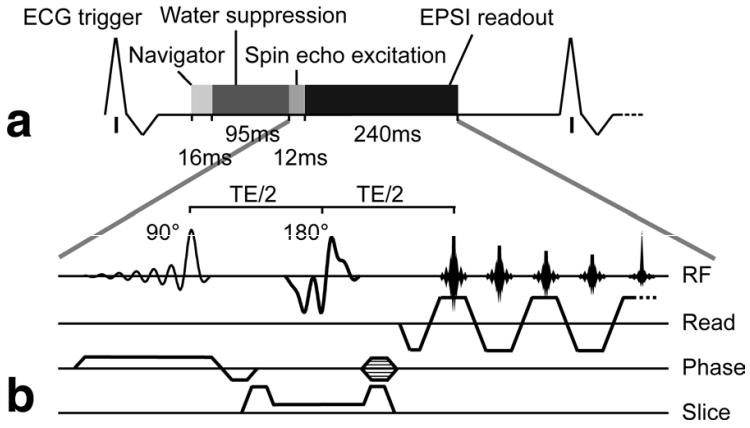


Figure 3.1: a: Schematic representation of the local-look navigator gated EPSI sequence. The ECG trigger is followed by the acquisition of the pencil beam navigator for respiratory motion compensation and the water-suppression pulses. The signal is acquired using an echo planar readout train. b: Schematic drawing of the spin echo-based orthogonal excitation using a 90° and a 180° pulse. The 90° excitation pulse is selective in phase encoding direction. Slice selection is achieved by the selective 180° refocusing pulse. The echo maximum is centered on the first readout of the echo planar readout train. The signal is sampled during gradient plateaus only.

outside the region of interest, FOX reduction based on an optimized selective excitation pulse in phase encoding direction and a slice selective refocusing pulse was implemented (Fig. 3.1b and Fig. 3.2 c,d).

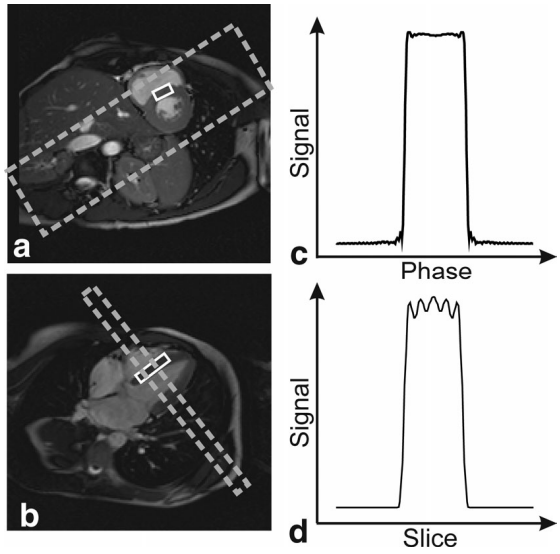


Figure 3.2: Position of the PRESS voxel (solid line) and the FOX of the EPSI acquisitions (dashed line). a: Short axis view with the limited FOX in phase encoding direction of the EPSI acquisitions. b: Four-chamber view with the EPSI slice prescribed. c: Excitation profile of the FOX in phase encoding direction. d: Refocusing profile in slice direction.

Pencil-beam navigator echoes were integrated for respiratory gating purposes. To minimize both scan time and residual respiratory motion, weighted gating was incorporated with a gating window of 4 and 3 mm for 70% of the outer k-space and 30% of the inner k-space, respectively. Water suppression was implemented using

two frequency selective excitation pulses each followed by a gradient spoiler just before signal excitation. ECG triggering during an end-systolic phase was used to have maximum thickening of the cardiac muscle, as can be seen in Fig. 3.2 a,b. In every experiment, water-suppressed and -unsuppressed EPSI data were acquired with a five-channel coil array .

## 3.3 EPSI Recostruction

A flow chart of the EPSI reconstruction steps with illustrations of their effect on water-unsuppressed data are shown in Fig. 3.3.

### 3.3.1 Coil combination

Coil sensitivity maps were calculated using the water-unsuppressed data. Taking into account the noise variances $\Psi_i$ of coil $i$, the sum-of-squares $SoS(\vec{x})$, and the phase-corrected signal maps $\Phi_i(\vec{x})$ at spatial positions $\vec{x}$ are given by:

$$\begin{aligned} SoS(\vec{x}) &= \sum_i \rho_i^{'}(\vec{x})^2 \\ \Phi_i(\vec{x}) &= \rho_i^{'}\Theta^*(\vec{x}) \\ \text{with } \Theta^*(\vec{x}) &= \sum_i \rho_i^{'}(\vec{x}) \end{aligned} \tag{3.1}$$

where $\rho_i^{'} = \psi_i^{-}1\rho_i$ refers to the noise variance weighted maximum signal in each coil's free induction decay (FID) and $^*$ denotes complex conjugate. Coil sensitivity maps $\S_i(\vec{x})$ can then be computed

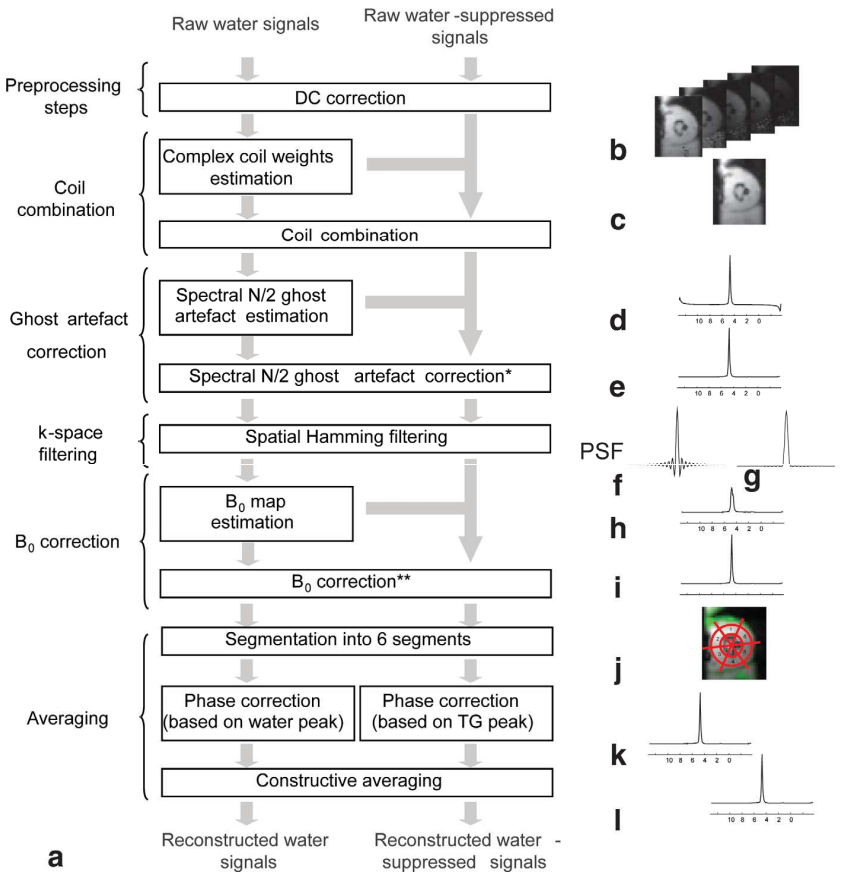


Figure 3.3: a) Flow chart of the EPSI reconstruction. Correction steps are shown for water-unsuppressed data in (b-l); (b) data before and (c) after coil combination, (d) spectrum before and (e) after spectral N/2 ghost correction, (f) spatial point-spread function (PSF) before and (g) after Hamming filtering, (h) spectrum before and (i) after B0 correction, (j) segmentation of the myocardium, and (k) spectrum before and (l) after phase correction.

according to:

$$S_i(\vec{x}) = \sqrt{\frac{\rho_i'(\vec{x})\rho_i'^*(\vec{x})}{\Phi_i(\vec{x})\Phi_i^*(\vec{x})SoS(\vec{x})}}\Phi_i(\vec{x}) \tag{3.2}$$

Using the coil sensitivity maps $S_i(\vec{x})$, the actual time domain signals $\rho_i\vec{x}, t$ of the water-suppressed and -unsuppressed EPSI data were combined using [31]:

$$\varsigma(\vec{x}, t) = \sum_i \rho_i(\vec{x}, t)S_i^*(\vec{x}) \tag{3.3}$$

### 3.3.2 Ghost correction

Spectral N/2 ghosts resulting from delays between even and odd readout gradients were corrected for by maximizing the water and fat signals in the water-unsuppressed scans [57]. The delays of the gradients cause a linear phase shift along the readout direction in image domain after spatial Fourier transformation according to the Fourier shift theorem. To estimate this phase shift, a trial set of phase shifts between 0 and $2\pi$ were applied to every second point of the FIDs to every pixel of the spectroscopic images, and the shift with the lowest N/2 ghost was detected. The estimated optimal phase shifts were then fitted with a linear function along the readout direction as, shown in Fig. 3.4.

Finally, the linear phase shifts were applied to every second readout of the FIDs to minimize the spectral N/2 ghosts in both the water-suppressed and -unsuppressed scans.

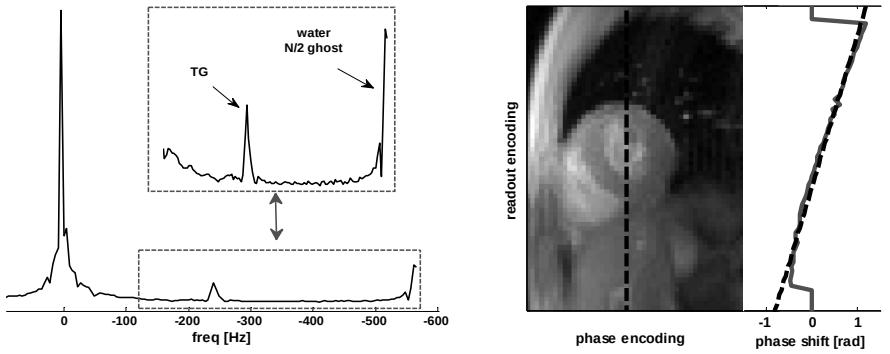


Figure 3.4: a) Example of spectral N/2 ghosts resulting from delays between even and odd readout gradients. (b) Linear fitting of the phase shifts along the readout direction.

### 3.3.3 Spatial filtering

To reduce effects of the point-spread function side lobes, k-space data were filtered using a Hamming function in the spatial dimensions resulting in an effective spatial resolution of $4.4 \times 4.4$ mm$^2$ [58].

### 3.3.4 B0 correction

For B0 correction, the position of the water and fat peaks was detected using a model spectrum for every pixel in the spectroscopic images of the water-unsuppressed scans. From the position of the water peak, B0 maps were estimated. Using the B0 maps, corrections were performed on a pixel-by-pixel basis using linear phase shifts applied to the time-domain signals of the water-suppressed and -unsuppressed signals.

### 3.3.5 Cardiac segmentation

For analysis, the myocardial muscle was divided into six segments (Fig. 3.5a,b). As spatial reference, the water image of the water-unsuppressed scan was used. A fat image from the water-suppressed scan was utilized as a second spatial reference (Fig. 3.5b) to accurately draw the epicardial contour, hence avoiding the contamination from epicardial fat in the segments.

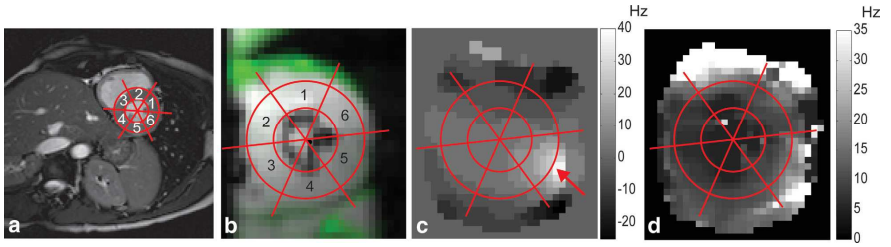


Figure 3.5: a) Six segments for the midcavity region. b) Water image from the non-water suppressed reference scan (gray) and a fat image from the water suppressed scan (green overlay). c) B0 map as estimated from the position of the water resonance in the water-unsuppressed scans. d) Linewidth map of the water resonance in the water unsuppressed scan.

### 3.3.6 Constructive averaging

To ensure phase coherent averaging, all spectra within each of the six regions of interest and all averages of the water-suppressed scans were phased using the fat resonance at 1.3 ppm [39]. The water-unsuppressed scans were phased using the first points of the FIDs. All spectra from the selected regions were subsequently averaged.

### 3.3.7 Quantification and statical analysis

For quantification of both the EPSI and the PRESS data, the resonance of trimethyl ammonium (TMA) compound at 3.2 ppm, the resonance of CR at 3.01 ppm, and the fat resonances at 2.1, 1.3, and 0.9 ppm in the water-suppressed spectra of the six defined segments were fitted using the AMARES function of the jMRUI software package [41,59]. Before fitting of the water-suppressed spectra, the residual water peak was filtered using a Hankel-Lanczos singular value decomposition method [60]. In addition, the water peak was fitted using AMARES in the same segments of the water-unsuppressed reference scans.

All estimated signal amplitudes were corrected for longitudinal and transversal relaxation effects and the Ernst angle excitation used for the water-suppressed EPSI scans. Relaxation values were taken from literature as follows: $T_1$ = 1100 ms and $T_2$ = 40 ms for myocardial water [15], T1  280 ms and T2  86 ms for TG estimated in skeletal muscle [42–44], and $T_1$ = 1500 ms and $T_2$ = 135 ms for myocardial CR [23, 42].

The TG signal was estimated as the sum of the fat resonances at 0.9 and 1.3 ppm [6]. TG and CR intensities were then calculated as a fraction of the unsuppressed water peak in the same region of interest. Moreover, the water peak was fitted on a voxel-by-voxel basis to assess the linewidth distribution of the waterline over the myocardial muscle.

For comparison of the quantification results of TG content with EPSI and PRESS, intraclass correlation coefficients (ICCs) were calculated using a mixed effect analysis of variance. To test differences

between mean values of linewidths and concentrations of the EPSI and PRESS measurements, a two-tailed paired t-test was used. A level of $P < 0.05$ was considered statistically significant. The analyses were performed using IBM SPSS (IBM SPSS, version 19; SPSS, Chicago, IL).

## 3.4 Motion effects in EPSI

The effect of cardiac motion on on signal encoding in EPSI sequence was investigated through numerical simulations. Indeed, since the EPSI sequence uses a bipolar gradient for simultaneous spatial-spectral encoding (as shown in Fig. 3.1), moving spins along the direction of the gradient accumulate a net phase that is linearly proportional to their velocity. To explore the influence of cardiac motion on signal encoding in the readout direction of the EPSI sequence, a Bloch's equations simulator has been developed.

### 3.4.1 EPSI Bloch simulator

The EPSI sequence was simulated using a geometrical model of the heart. The contraction of the left ventricle has been simulated with a ring model used to reproduce wall thickening and heart rotation, as described in [61]. Static field (B0) maps have been used to simulate magnetic field inhomogeneity. Cardiac motion *during* gradients was neglected given the short duration of each individual gradient ($< 1$ ms), while motion *between* gradients was considered. To this end, the heart phase of the geometrical model was changed during the train of bipolar gradients as shown in Fig 3.6.

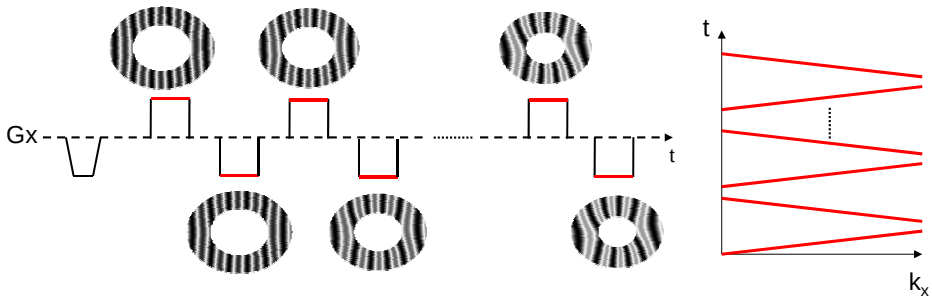


Figure 3.6: Geometrical model used to simulate cardiac motion during the readout ($G_x$) gradient of the EPSI sequence.

EPSI datasets were simulated by computing the signal evolution in k-space domain as following:

$$S(k_{FE}, k_{PE}) = \int_x \int_y e^{\frac{-t}{T2^*}} \rho(x,y) e^{j2\pi(k_{FE}x + k_{PE}y)} e^{j2\pi f(x,y)t} \qquad (3.4)$$

where $k_{FE}$ and $k_{PE}$ are the k-space coordinates in the frequency (FE) and phase encoding (PE) direction, $\rho(x,y)$ is the map of metabolite amplitudes, and $f(x,y)$ is the spatial distribution of resonance frequencies.

Table 3.1: Metabolite parameters used in the EPSI simulation.

| Peak | frequency (Hz) | T2* (ms) | $\rho$ (a.u.) |
|---|---|---|---|
| Water | 0 | 45 | 100 |
| TG | 220 | 25 | 0.5 |

The simulated EPSI datasets were reconstructed using the processing steps described in section 3.3. Fitting estimates were used to quantify the influence of heart motion on water and fat resonance parameters (amplitude, linewidth and resonance frequency).

## 3.5 Results

### 3.5.1 Experimental protocol

The parameters of the EPSI sequence were as follows: field of view $300 \times 150\ mm^2$, FOX 65-85 mm, nominal resolution $3 \times 3\ mm^2$ , slice thickness 15 mm, spectral bandwidth 1064 Hz, spectral resolution 4.2 Hz, echo time (TE) 12 ms, pulse repetition time (TR) 750-1250 ms depending on heart rate, eight signal averages for water suppressed scans, and nominal acquisition time for water-suppressed/–unsuppressed scans: 6:40 / 0:50 min resulting in a total acquisition time of about 18:45 min with a navigator efficiency of 40%.

The cardiac trigger delay to peak systole was estimated using cine scans at approximately 320 ms after the R-wave. To optimize signal-to-noise ratio of the CR resonance at 3.01 ppm, Ernst angle excitation for the water-suppressed scans was used leading to an excitation angle of 115-125° combined with the 180° refocusing pulse, depending on heart rate.

For comparison, a navigator gated and cardiac triggered point-resolved spectroscopy (PRESS) sequence was implemented and applied in the same session ( [6]). Both water and water-suppressed spectra were acquired. To avoid contamination from epicardial fat, the single voxel was placed in the septum (Fig. 3.2 a,b.). For PRESS, only data from this single position were acquired. The parameters of the PRESS sequence were as follows: voxel size $10 \times 20 \times 40\ mm^3$, TE/TR 33/2000 ms, 128 signal averages for water suppressed and eight signal averages for the water unsuppressed scans. Nominal acquisition time for water-suppressed/-unsuppressed scans: 4:16/0:16

min, resulting in a total acquisition time of 11:20 min with a gating efficiency of 40%.

For all experiments, the body coil was used for signal excitation and a five-channel cardiac array was used for signal reception. A total of 12 healthy volunteers (mean age: 29 years; range 23-46 years) were measured after informed consent was obtained according to institutional guidelines.

### 3.5.2 Simulation results

Figure 3.7 shows the simulation results of the EPSI sequence. Without motion (upper panels of Fig. 3.7), fitting results were consistent with the resonance parameters imposed in the simulation (see Tab. 3.1), estimated TG content of 0.483 ± 0.003a.u., and linewidths of 7.7 ± 0.2 Hz.

In presence of motion (lower panels of Fig. 3.7), a small underestimation of the TG/W percentage (0.462 ± 0.010) was observed, which was associated to increased linewidths (10.3 ± 1.6 Hz), especially in the readout direction. Also, a small variation of the frequency difference between water and TG peaks was found in the readout direction (219.95 ± 0.76).

### 3.5.3 *In-vivo* results

Results of the reconstruction steps are shown in Fig. 3.8. Spectral N/2 ghosts were reduced by 90.9 ± 6.1% (Fig. 3.8b,c) resulting in a remaining ghost signal of 1.54 ± 0.57% of the water-peak height.

Line broadening due to B0 inhomogeneity in the regions of inter-

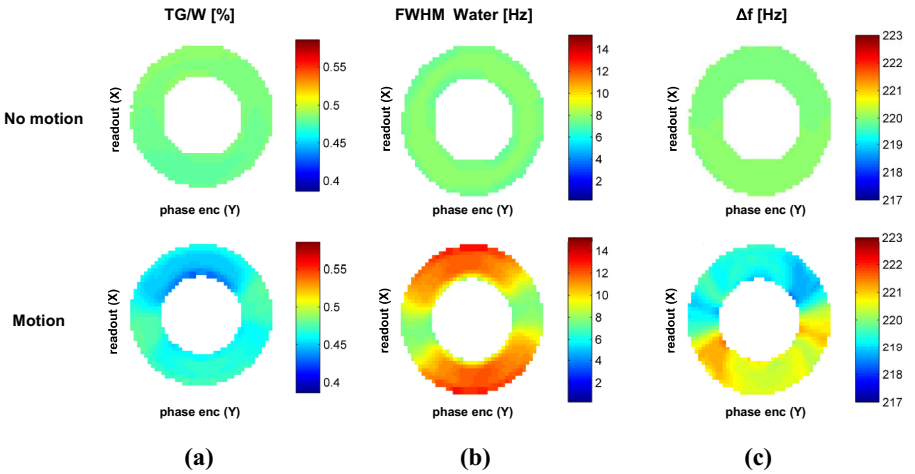


Figure 3.7: EPSI simulation results. a) TG content (TG/W) expressed as percentage of water fraction. b) Linewidth of the water peak expressed as Full-Width at Half Maximum (FWHM). c) Frequency difference between water and TG peak.

est was reduced from 12.3 ± 3.8 to 9.7 ± 1.8 Hz (Fig. 3.8a,c). Overall field map values across the myocardium showed variations of 29.6 ± 7.6 Hz (Fig. 3.5c). However, the actual linewidths of the water-unsuppressed resonance in the individual voxels varied between 5 and 25 Hz (Fig. 3.5d).

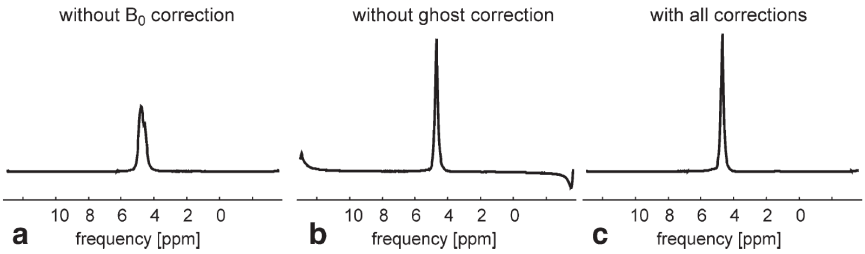


Figure 3.8: Water-unsuppressed spectra of one segment in the lateral wall of the EPSI scans showing different reconstruction steps of the EPSI data. a) Spectrum without the B0 correction step, (b) without spectral N/2 ghost correction, (c) with all correction steps.

Linewidth variations in the six regions of interest from the EPSI data and the single voxel of the PRESS scan across all 12 subjects are shown in Table 3.2. The small linewidths and the small variations in the septal region (segment 2 and 3) allowed for detection and a good discrimination of the resonances of TMA at 3.2 ppm and CR at 3.01 ppm. However, the increased linewidths and variations in the lateral segments 5 and 6 caused a degradation of the spectral quality in these regions. In particular, the linewidths of the water resonance were significantly higher in the lateral segment 5 compared to every other segment.

Figure 3.9 shows spectra from six regions of interest located in the

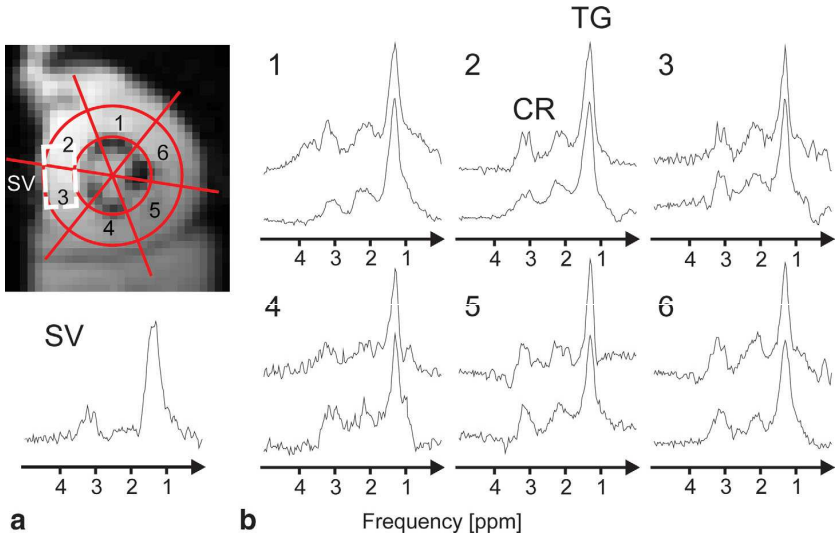


Figure 3.9: (a) PRESS (SV) and EPSI regions of interest. b) Spectra from the regions of interest indicated in (a) in test-retest reliability study on a single volunteer.

midcavity region of the heart and a PRESS spectrum from the septal wall for comparison. Spectra from two measurements of a single volunteer are shown for every segment. Between the two scans, the subject was taken out of the scanner and subsequently repositioned.

The mean values of all segments for the two measurements were 0.42 ± 0.06% and 0.41 ± 0.08% for TG content and 0.063 ± 0.025% and 0.081 ± 0.024% for CR content. The spectral quality of the EPSI spectra was found to be comparable to the PRESS spectrum in the septum (Fig. 3.9).

Table 3.2: Measured Line Width (Hz) of the Water Resonance in Water-Unsuppressed EPSI Reference Scans for the Six Regions of Interest (Fig. 3.5a,b) and of the PRESS Measurements (N = 12).

| Segment | Mean over subjects | Mean over intrasubjects SD |
|---|---|---|
| 1 | 9.0 ± 1.6 | 2.70 ± 0.91 |
| 2 | 9.1 ± 1.5 | 2.08 ± 0.91 |
| 3 | 8.7 ± 1.0 | 1.94 ± 0.54 |
| 4 | 9.6 ± 1.3 | 2.11 ± 0.69 |
| 5 | 11.6 ± 2.3 | 3.33 ± 1.65 |
| 6 | 10.2 ± 1.6 | 2.42 ± 0.61 |
| PRESS | 11.2 ± 1.8 | - |

Mean values overall subjects and mean values of the SD across voxels of the individual subjects are shown for the EPSI data.

Table 3.3: EPSI and PRESS quantification results for each subject.

| | TG/W % | | | CR/W % | | |
|---|---|---|---|---|---|---|
| Sub. | EPSI mean | EPSI septum | PRESS | EPSI mean | EPSI septum | PRESS |
| 1 | 0.40 ± 0.10 | 0.45 | 0.47 | 0.09 ± 0.02 | 0.08 | 0.06 |
| 2 | 0.39 ± 0.07 | 0.45 | 0.59 | 0.08 ± 0.03 | 0.11 | 0.09 |
| 3 | 0.32 ± 0.05 | 0.34 | 0.47 | 0.06 ± 0.02 | 0.06 | 0.08 |
| 4 | 0.71 ± 0.09 | 0.73 | 0.77 | 0.09 ± 0.05 | 0.10 | 0.08 |
| 5 | 0.36 ± 0.08 | 0.37 | 0.68 | 0.06 ± 0.03 | 0.04 | $-^{a}$ |
| 6 | 0.68 ± 0.14 | 0.69 | 0.59 | 0.05 ± 0.04 | 0.04 | 0.06 |
| 7 | 0.56 ± 0.16 | 0.72 | 0.75 | 0.07 ± 0.03 | 0.09 | 0.10 |
| 8 | 0.25 ± 0.07 | 0.30 | 0.25 | 0.05 ± 0.02 | 0.03 | 0.05 |
| 9 | 0.16 ± 0.05 | 0.18 | 0.31 | 0.02 ± 0.01 | 0.02 | 0.09 |
| 10 | 0.39 ± 0.06 | 0.43 | 0.39 | 0.03 ± 0.02 | 0.07 | 0.05 |
| 11 | 0.39 ± 0.06 | 0.47 | 0.39 | 0.04 ± 0.02 | 0.06 | 0.06 |
| 12 | 0.51 ± 0.11 | 0.64 | 0.53 | 0.04 ± 0.01 | 0.04 | 0.06 |
| Mean | 0.43 ± 0.16 | 0.48 ± 0.18$^{c}$ | 0.52 ± 0.17$^{c}$ | 0.06 ± 0.02 | 0.06 ± 0.03$^{d}$ | 0.07 ± 0.02$^{b,d}$ |

For EPSI mean values, overall segments are shown. Values for TG content (TG/W) and CR content (CR/W) are given as percentage of water fraction after T1 and T2 correction. $^{a}$CR was not found in this spectrum. $^{b}$Average and SD of 11 volunteers. $^{c,d}$ No significant differences have been found ($P > 0.05$).

Table 3.4: Quantification Results for the Different Segments for EPSI and Single Septal PRESS Voxel.

| Segment | TG/W % | $ICC_{PRESS}$ | TG/W % | N[a] |
|---|---|---|---|---|
| 1 | 0.45 ± 0.20 | 0.64 | 0.04 ± 0.03 | 10 |
| 2 | 0.52 ± 0.21 | 0.72 | 0.07 ± 0.03 | 11 |
| 3 | 0.44 ± 0.16 | 0.67 | 0.06 ± 0.03 | 12 |
| 4 | 0.42 ± 0.21 | 0.65 | 0.06 ± 0.03 | 9 |
| 5 | 0.37 ± 0.14 | 0.34 | 0.07 ± 0.05 | 11 |
| 6 | 0.36 ± 0.16 | 0.52 | 0.06 ± 0.04 | 12 |
| PRESS | 0.52 ± 0.17 | – | 0.07 ± 0.02 | 11 |

Values for TG content (TG/W) and CR content (CR/W) are given as percentage of water fraction. ICC to PRESS is given.
[a]Number of volunteers where CR was successfully fitted using jMRUI

The quantification results of all 12 volunteers are summarized in Tab. 3.3 and Tab. 3.4. The ICC for the TG content estimated with PRESS and EPSI was found to be 0.72 (95% confidence interval: 0.27, 0.91; $P < 0.004$) for the septal segment 2 and 0.67 (95% confidence interval: 0.12, 0.90; $P < 0.001$) for the mean overall segments. Within the subjects, a mean coefficient of variation of 21 ± 6% was found for the different segments.

Because of line broadening in the lateral wall and the region of the posterior vein of the left ventricle (Fig. 3.5c), spectra from the lateral segments 5 and 6 revealed lower effective spectral resolution and a lower spectral quality.

Moreover, coil sensitivities were lowest in this region (Tab. 3.5). As a result, the correlation and significance of the correlation rel-

Table 3.5: Comparison of sensitivity in the six myocardial segments.

| Segment | Relative SNR[a] |
|---|---|
| 1 | 0.91 ± 0.13 |
| 2 | 1 |
| 3 | 0.88 ± 0.12 |
| 4 | 0.70 ± 0.08 |
| 5 | 0.68 ± 0.10 |
| 6 | 0.81 ± 0.11 |

[a]Relative SNRs are calculated from water-unsuppressed signals and compared with segment 2, which had the highest mean SNR.

ative to the PRESS measurements found for segment 5 (ICC 0.32, 95% confidence interval: -0.29, 0.74; $P < 0.05$) was comparably low Tab. 3.4. No significant differences were found between the septal region of the EPSI (segments 2 and 3) and the PRESS scans, demonstrating good agreement of the two measurements ($P = 0.35$ for TG, $P = 0.40$ for CR, Tab. 3.3). However, significant differences were detected between the mean of all segments of the EPSI measurements and the PRESS measurements in the septal region ($P = 0.021$). The lower mean TG content measured with EPSI indicates that the EPSI measurements underestimate the TG content compared with the PRESS measurements.

## 3.6 Discussion

An optimized EPSI sequence has been proposed to map relative CR and TG content in the heart in a study including 12 healthy

volunteers.

EPSI spectra showed significant correlation with single-voxel data acquired in the septum for all segments. The values measured for TG with EPSI and PRESS agree with values reported earlier by van der Meer et al. [6].

The CR content as measured in this study, however, was found to be lower compared with previous data from single voxel measurements [3, 23]. Although T1 and T2 was not measured in this study, absolute CR concentrations, based on a mean tissue water content of 76.4% [3], literature T1 and T2 values [15, 23, 42–44], and nominal scanner flip angles, are projected to be about 17.2 ± 8.6 $\mu$mol/g and 20.0 ± 5.7 $\mu$ol/g wet weight for EPSI and PRESS, respectively. These values are smaller than previous estimates of 28 ± 6 $\mu$mol/g [3] and 28.9 ± 4.4 $\mu$mol/g wet weight [23] possibly reflecting uncertainties in the relaxation corrections, differences between time and frequency domain spectral analysis and partial contamination of the CR signal if the TMA resonance at 3.2 ppm is not fitted independently. However, when comparing the data of this work against biochemical analysis of CR concentrations (17.9 $\mu$mol/g [62] and 20.8 ± 4.5 $\mu$mol/g [63]) very good correspondence is noted.

The lateral segment in the region of the posterior vein of the left ventricle was found to be compromised with significantly lower correlation when compared with both EPSI and PRESS data from the septal region. This finding is associated with strong B0 inhomogeneities induced by the vicinity of deoxygenated blood inside the posterior vein. Significant stronger line broadening compared with all other segments was detected in the related segment 5 (11.6 ± 2.3

Hz, Tab. 3.2) in agreement with previous data by Reeder et al. [64]. B0 inhomogeneities also compromised the individual estimation of TMA and CR resonances.

These resonances are separated by 0.19 ppm, which corresponds to 12.1 Hz at 1.5 T. Furthermore, coil sensitivity drop-off due to greater distance between the lateral wall and the coil array (Tab. 3.5) relates to the reduced sensitivity in the lateral area. Relative to the anteroseptal segment, the signal-to-noise ratio in the posterolateral segment was reduced by 30%.

Overall, shimming was found to be a limiting factor. Voxel volumes were 0.290 mL for EPSI and 8 mL for PRESS. Accordingly, significantly smaller linewidths were detected in the septal region for the EPSI scan compared with the PRESS scans (Tab. 3.2). With the availability of higher order shims, the linewidth limitations in the regions of the lateral wall and the posterior vein of the left ventricle can be addressed in future work. Multiple channel coil arrays are expected to leverage the limited sensitivity in lateral and posterior regions alongside translating the work to higher B0 field strengths. High-field application will also improve the separation of the TMA and CR resonances, which was found to be limiting in this study at 1.5 T.

The quantification of TG and CR was corrected for longitudinal and transversal relaxation effects based on literature values for T1 and T2. The effect of T2 correction on the quantitative results was found to be small for EPSI given the short TEs used. The TE of the double spin echo PRESS sequence, however, was almost three times longer and hence inaccuracies in T2 may have resulted in significant differences in the quantitative results of the PRESS measurements.

The T2 correction factors for TE of 33 ms (PRESS) / 12 ms (EPSI) did change relative TG and CR content by 36%/15% and 44%/19%, respectively. Assuming a 10% uncertainty in T2, the correction factors for PRESS/EPSI are offset by 12%/5% and 11%/4% for TG and CR and thus may explain in parts the difference seen between PRESS and EPSI in the septal region. Correction for longitudinal relaxation did change the relative TG and CR content by $26 \pm 5\%$ and $9 \pm 4\%$ depending on heart rate. A 10% uncertainty in the estimated T1 relaxation time would result in an offset for TG and CR content of 6.7 and 11%, respectively. As the influence of T1 relaxation for EPSI and PRESS is comparable, differences of TG and CR content measured with EPSI and PRESS are not explained by the uncertainty in T1 values. However, they may partly explain differences compared with CR content reported in the literature [3,23]. In other applications, it was demonstrated that corrections for longitudinal and transversal relaxation effects can introduce systematic errors [42,43]. Accordingly, subject-specific measurements of relaxation constants seem warranted and need to be included in future studies.

The variance found across all segments of the EPSI data is attributed in parts to the reduced coil sensitivity for lateral and posterior segments and to a loss in spectral resolution given strong B0 gradients in particular close to the posterior vein of the left ventricle.

In summary, the presented EPSI technique allows assessing myocardial CR and TG content from several regions of interest in reasonable scan times, thus demonstrating to be a promising tool for investigating spatial alterations of myocardial metabolism.

# Chapter 4

# Myocardial T1 mapping

Besides magnetic resonance spectroscopy (MRS), quantitative magnetic resonance imaging (MRI) techniques based on relaxation times mapping provide fundamental information for myocardial tissue characterization. Longitudinal relaxation time (T1) is altered in various cardiac diseases like myocardial infarction and diffuse fibrosis. T1 quantification is based on the acquisition of a series of images that sample the recovery curve of the longitudinal relaxation. Several pulse sequence have been proposed to collect images suitable for pixel-wise T1 mapping. However, differences in T1 values obtained either from different protocols or from different regions of the myocardium have not been well investigated, especially at 3.0 T. The objective of this study is to implement and optimize a pulse sequence for myocardial T1 mapping at 3.0 T.

## 4.1 Myocardial T1 measurement

Longitudinal relaxation time or spin-lattice relaxation time (T1) is the time constant that rules the exponential recovery of longitudinal magnetization equilibrium. Since T1 relaxation time depends on the chemical and physical environments of water protons [15], T1 values vary significantly among different tissues, but also among different physiopathological conditions in the same tissue. Examples of physiopathological processes that cause T1 changes are inflammation, infarction, edema and fibrosis [15].

T1 relaxation time can also be altered artificially by injecting contrast media. Gadolinium-based contrast agents (GBCA) shorten T1 in tissues where are accumulated, thus producing postcontrast T1-weighted images with enhanced signals in these tissues. The late gadolinium enhancement (LGE) technique is now routinely used in cardiac MRI to detect myocardial infarction (MI). Indeed, fibrotic tissues experience a prolonged wash-out of the gadolinium, leading to bright signal intensity in conventional inversion-recovery (IR) gradient echo images [65]. However, there are two main limitations of the LGE technique. Firstly, the degree of enhancement also depends on the inversion time (TI)of the IR sequence chosen for nulling the signal of noninfarcted myocardium [66]. Secondly, diffuse myocardial fibrosis is more difficult to assess with LGE since image contrast relies on the difference in signal intensity between fibrotic and "normal" myocardium, and such differences is eliminated when the process is diffuse [67].

To overcome these limitations new approaches for the quantitative measurement of myocardial T1 have been developed. In gen-

eral, a method for T1 quantification is based three main steps: 1) the perturbation of the longitudinal magnetization using either a 180° (inversion) or a 90° (saturation) radiofrequency pulse; 2) the acquisition of a series of images that sample the recovery curve of the longitudinal relaxation; 3) the fitting of the sampled curve with a proper T1-recovery mathematical model for the extraction of the T1 value.

The cine inversion recovery approach (Cine-IR) is based on the application of a inversion pulse is followed by a fast a cine acquisition where each cardiac phase experiences a different time delay after the inversion pulse and thus a different T1 weighting [68]. Although Cine-IR was shown to be reliable in the estimation of myocardial T1 values after contrast agent administration, this method only allows a region of region of interest (ROI) analysis rather than a pixel-by-pixel T1 fitting [16]. The first successful implementation of myocardial pixel-wise T1 mapping was based on the Modified Look-Locker Inversion Recovery (MOLLI) pulse sequence [17]. MOLLI sequence allows the acquisition of several images at different inversion times but in the same cardiac phase and in a single breath-hold. Thus, the spatial co-registration of the acquired images allows to perform the signal fitting for the T1 quantification in a pixel-wise fashion, i.e. T1 mapping.

The MOLLI approach inspired the development of several methods for T1 mapping based on either on inversion recovery [18] or saturation recovery sequences [19]. The aim of this study is to implement and optimize through numerical simulations a pulse sequence based on MOLLI for myocardial T1 mapping at 3.0 T.

## 4.2 MOLLI sequence

The MOLLI pulse sequence was implemented on a 3.0 T Philips Ingenia system (Philips Healthcare, Best, The Netherlands). The sequence consists of three Look-Locker experiments, i.e. three inversion pulses each followed by the single-shot acquisitions triggered at a fixed cardiac phase in successive heartbeats. The single-shot acquisition is performed with a balance steady state free precession (b-SSFP) sequence [69].

The number of images acquired after each of the three inversion pulses is three, three and five respectively (3-3-5 scheme), yielding a total of eleven images, each one acquired with a different inversion time. In the original version of MOLLI, a resting period of three heartbeats is inserted before the next inversion pulse to allow the recovery of the longitudinal magnetization [17]. This causes a significant dependence of the magnetization, and hence of the T1 estimation, on the heart rate. To reduce this effect, the implemented MOLLI sequence implemented in this study adopted a resting period independent on the heart rate, by setting a minimum delay of six seconds between inversion pulses.

Figure 4.1 shows the implemented MOLLI sequence. In each $k$ Look-Locker experiment, the effective inversion time $t$ of each image depends on the delay time between the inversion pulse and the acquisition in the first heartbeat ($TI_k$) and on the RR interval for the successive $n$ heartbeats according to:

$$t = TI_k + (n-1)\text{RR interval} \tag{4.1}$$

where $TI_k$ was set to 100 ms, 200 ms and 350 ms for $k = 1, 2, 3$

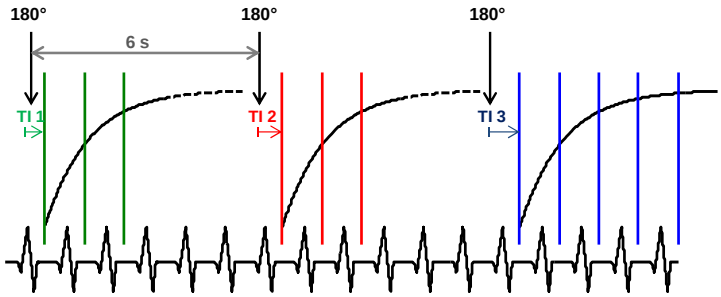


Figure 4.1: Schematic representation of the MOLLI pulse sequence. A minimum delay of six second was set between the inversion pulses.

respectively.

The images are then sorted by their effective inversion time before pixel-wise fitting. Figure 4.2 shows a schematic representation of the MOLLI method for T1 mapping. The three sets of images that sample the recovery curve of the longitudinal magnetization are merged in a single set according to their effective inversion time.

The three-parameter monoexponential model used for T1 estimation is the following:

$$y = A - Be^{-t/T_1^*} \tag{4.2}$$

where $y$ is the pixel intensity of the MOLLI images and $T_1^*$ is called apparent T1. Since pixel intensities can assume only positive values in magnitude MR images, the sign for negative values of the magnetization need to be restored. To identify these values, the fitting procedure was repeated changing iteratively the sign of the first images. The fitting result with the minimum residual error was chosen to correct the signal polarity [70].

To take into account that the recovery curve of the longitudinal

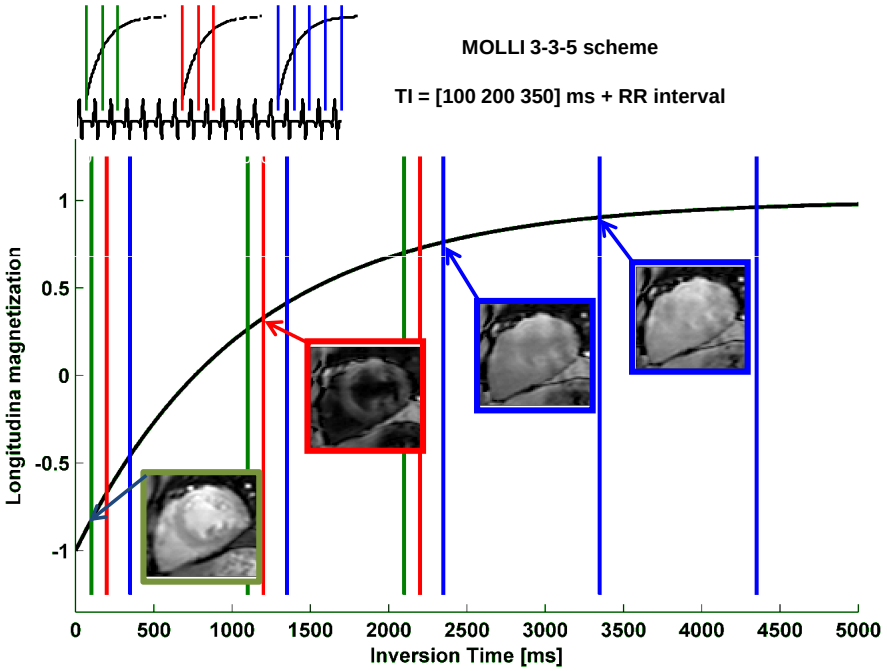


Figure 4.2: Schematic representation of the MOLLI method for T1 mapping.

magnetization is perturbed by the readouts used for image acquisition, the Look-Locker correction [17] was then applied according to the following formula:

$$T_1 = T_1^* \left( \frac{B}{A} - 1 \right) \tag{4.3}$$

where T1 is the corrected estimated of the T1 relaxation time constant.

## 4.3 Bloch simulation

In order to investigate the influence of different parameters (flip angle, TR/TE, k-space sampling, B0-field inhomogeneity) of the implemented MOLLI sequence on T1 estimation, a Bloch's equation simulator was developed. The simulation calculated the magnetization during the MOLLI experiment, taking into account both the spin evolution during each single-shot SSFP readout and relaxation between SSFP readouts.

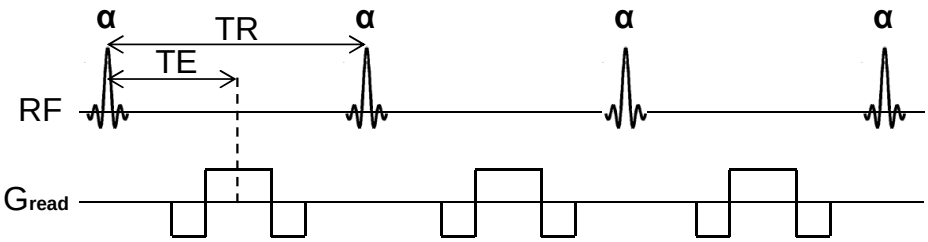


Figure 4.3: Schematic representation of the SSFP readout used for MOLLI image acquisition.

A simplified version (without slice and phase encoding gradients) of the SSFP readout is shown in Fig. 4.3. The single-shot SSFP read-

out is composed by a train of low flip angle $\alpha$ radiofrequency pulses at a repetition time (TR) distance. The echo time (TE) corresponding to the center of each k-space line is equidistant between $\alpha$ pulses, i.e. TR/2. As shown in Fig. 4.3 in SSFP the readout gradient is balanced, that is the area of the positive lobe is equal to area of the negative lobes.

The evolution of the magnetization during the SSFP readout was calculated using the framework described in [71].

The rotation matrix that describe the RF nutation about the $x$-axis by an angle $\alpha$ is the following:

$$\mathbf{R}_\alpha = \begin{bmatrix} 1 & 0 & 0 \\ 0 & \cos\alpha & \sin\alpha \\ 0 & -\sin\alpha & \cos\alpha \end{bmatrix} \tag{4.4}$$

Between $\alpha$ excitation the magnetization undergoes a precession by an angle $\theta = 2\pi\Delta f \mathrm{TR}$ about the $z$-axis, where $\Delta f$ is the spin off-resonance due to B0-inhomogeneity. The rotation matrix that describes the precession over a period $\tau$ is:

$$\mathbf{P}(\tau) = \begin{bmatrix} \cos(2\pi\Delta f\tau) & \sin(2\pi\Delta f\tau) & 0 \\ -\sin(2\pi\Delta f\tau) & \cos(2\pi\Delta f\tau) & 0 \\ 0 & 0 & 1 \end{bmatrix} \tag{4.5}$$

The T1 and T2 relaxation over a period $\tau$ can be represented by a multiplication by the matrix:

$$\mathbf{C}(\tau) = \begin{bmatrix} e^{-\tau/T_2} & 0 & 0 \\ 0 & e^{-\tau/T_2} & 0 \\ 0 & 0 & e^{-\tau/T_1} \end{bmatrix} \tag{4.6}$$

and an addition of the vector:

$$\mathbf{D}(\tau) = (\mathbf{I} - \mathbf{C}(\tau)) \begin{bmatrix} 0 \\ 0 \\ M_0 \end{bmatrix} \tag{4.7}$$

Using this notation, it has been shown [71] that the magnetization change from one excitation to the following can be expressed in the form of a discrete-time system:

$$\mathbf{M}_{k+1} = \mathbf{A}\mathbf{M}_k + \mathbf{B} \tag{4.8}$$

where $\mathbf{M}_k$ is a 3D vector representing the magnetization at the $k$-th excitation $(M_x, M_x, M_z)$, $\mathbf{A}$ is a 3 x 3 matrix $\mathbf{A} = \mathbf{P}_1\mathbf{C}_1\mathbf{R}_\alpha\mathbf{P}_2\mathbf{C}_2$ and $\mathbf{B}$ is a 3D vector $\mathbf{B} = \mathbf{P}_1\mathbf{C}_1\mathbf{R}_\alpha\mathbf{D}_2 + \mathbf{D}_1$, where

$$\begin{aligned} \mathbf{P}_1 &= \mathbf{P}(\mathrm{TE}) \quad \text{and} \quad \mathbf{P}_2 = \mathbf{P}(\mathrm{TR} - \mathrm{TE}) \\ \mathbf{C}_1 &= \mathbf{C}(\mathrm{TE}) \quad \text{and} \quad \mathbf{C}_2 = \mathbf{C}(\mathrm{TR} - \mathrm{TE}) \\ \mathbf{D}_1 &= \mathbf{D}(\mathrm{TE}) \quad \text{and} \quad \mathbf{D}_2 = \mathbf{D}(\mathrm{TR} - \mathrm{TE}) \end{aligned}$$

To reduce transient oscillations of the magnetization at the beginning of the SSFP readout, a series of dummy excitations was included in the simulation. To this end, two different preparation scheme were simulated: the $\alpha/2$ train [69] and the linear flip angle (LFA) preparation [72].

For T1 estimation, the value of the longitudinal magnetization at the $k$-th excitation corresponding to the central k-space line was used as input of the three-parameter model fitting described by Eq. 4.2.

## 4.4 Results

### 4.4.1 Simulation results

Figure 4.4 shows the evolution of the longitudinal magnetization during the MOLLI experiment for three different values of the flip angle $\alpha$ (15°, 30° and 45°). The recovery of the of the longitudinal magnetization after each inversion pulse is perturbed by the SSFP readouts used for the image acquisition. This perturbation becomes noticeable as the flip angle increases.

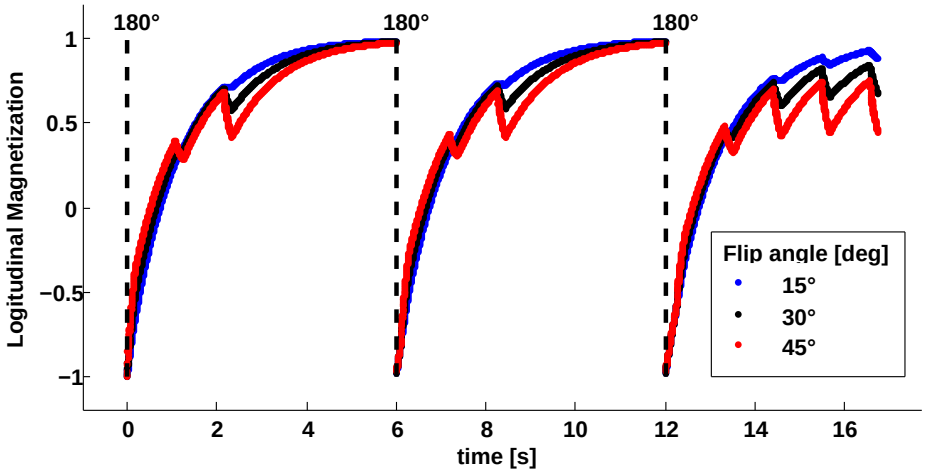


Figure 4.4: Evolution of the longitudinal magnetization during three MOLLI experiments with different flip angle.

A detailed representation of the evolution of the longitudinal magnetization during a SSFP readout is shown in Fig. 4.5. As depicted, initial $\alpha-$excitations are characterized by remarkable transient oscillations. The use of dummy excitations with the $\alpha/2$ train or the LFA preparation largely reduce the oscillations, thus accel-

erating the reaching of a *transient* steady state. In the following simulations, the LFA was adopted because of its robustness to field inhomogeneities [72], a feature extremely important at 3T.

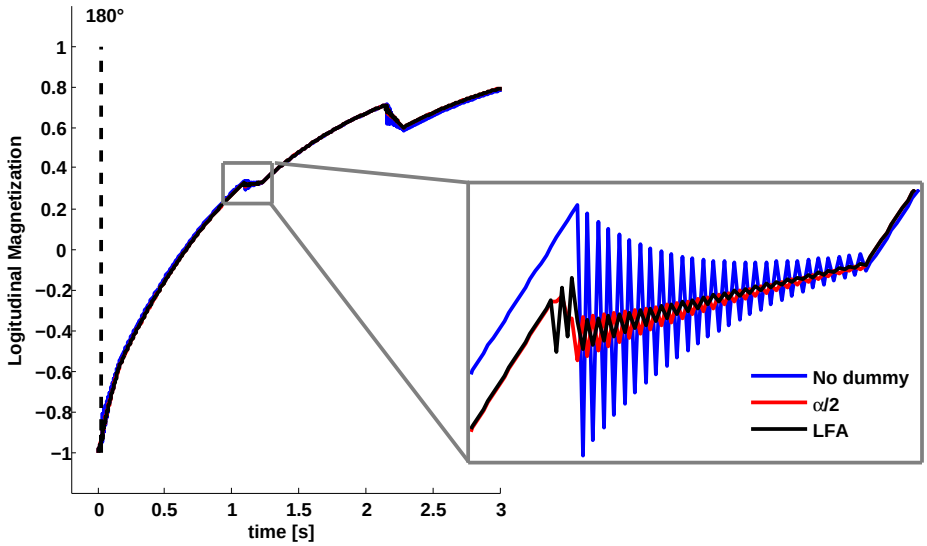


Figure 4.5: Reduction of transient oscillations using $\alpha/2$ and linear flip angle preparation schemes.

Figure 4.6 shows the results obtained by the MOLLI simulation using two different resting periods between the Look-Locker (LL) experiments of the 3-3-5 scheme (see Fig. 4.1): *3 RR* and *6 sec*. In the first case three heartbeats separate the last readout of a LL and the inversion pulse of the successive LL (as in original version of MOLLI, see Ref. [17]). In the second case, a minimum delay of six seconds is retained between two inversion pulses. The *6 sec* approach achieved a smaller error percentage in T1 estimation than *3 RR*, especially for increasing values of T1 as shown in Fig. 4.6 (a). In addition, this approach was demonstrated to be more insensitive

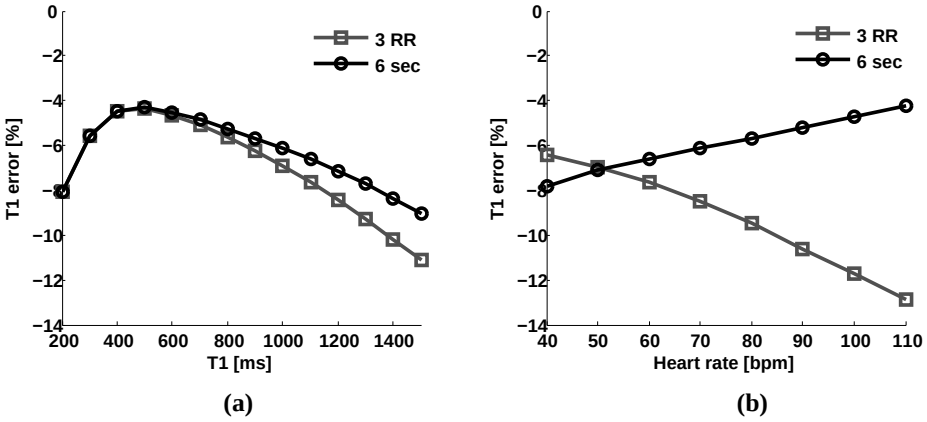


Figure 4.6: Comparison between *3 RR* and *6 sec* resting periods. (a) Error in T1 estimation as a function of the real T1 of the simulated tissue (HR=60 bpm). (b) Error in T1 estimation as a function of the heart rate (T1=1100 ms).

to the heart rate (HR), providing accurate results even for elevated values of the cardiac frequency, as shown in Fig. 4.6 (b).

The influence of the flip angle $\alpha$ of the SSFP readout in T1 estimation is shown in Fig. 4.7. A systematic underestimation of T1 was observed for all T1 values. This systematic underestimation can be explained by the fact that the longitudinal relaxation curve more rapidly reaches an asymptotic value due the perturbation of the SSFP readouts, as shown in Fig. 4.4. Notably, this negative bias increased with larger flip angles. Although, very low flip angles provide the most accurate T1 estimation, limitations in terms of SNR lead to the choice of flip angles not below 20°.

The influence of of the SSFP readout was also found to be T2-dependent, as shown in the simulation results of Fig. 4.8, where the

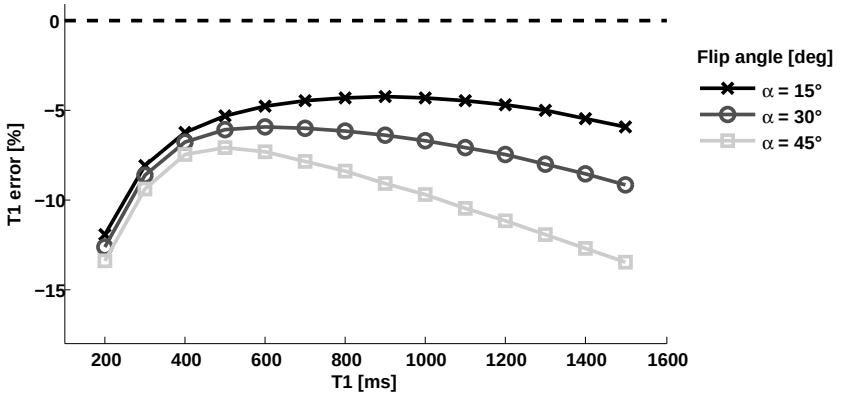


Figure 4.7: Influence of flip angle $\alpha$ of the SSFP readout in T1 estimation. The negative bias of T1 estimation increases with larger flip angles.

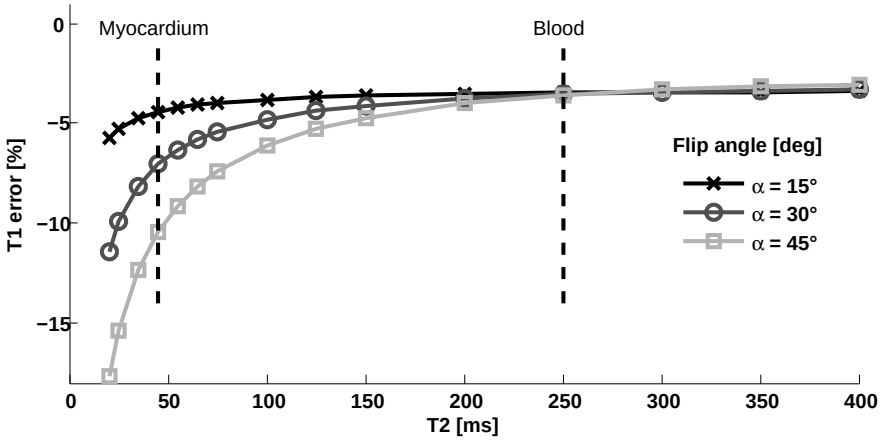


Figure 4.8: T1 underestimation due to the perturbation of the SSFP readout increases for shorter T2 (T1=1100 ms, HR=60 bpm).

T1 underestimation increased for shorter T2 values. This resulted in a larger negative bias of the myocardial tissue (about 7% with $\alpha = 30°$), which normally has T2=45 ms [73], compared to the blood tissue (about 3% with $\alpha = 30°$), which has T2 of 250 ms.

### Off-resonance effects

Since balance–SSFP sequences are typically influenced by off-resonances, i.e. spins with different resonance frequencies due to local static B0-inhomogeneities, the sensitivity of the MOLLI sequence to off-resonance effects was investigated.

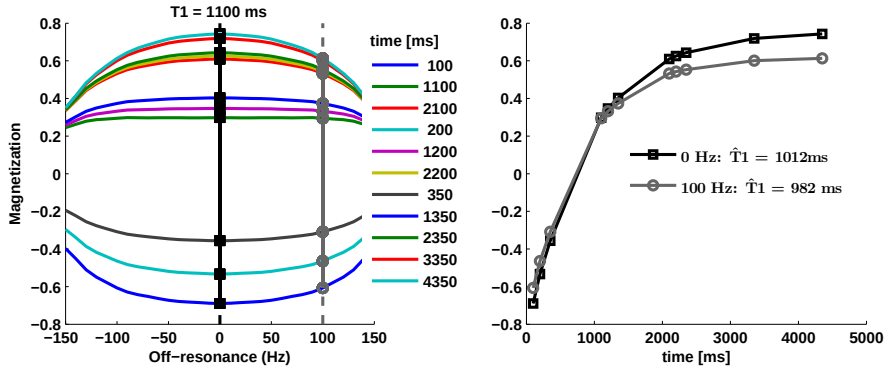


Figure 4.9: (a) Magnetization of the MOLLI images as a function of the off-resonance frequencies for a T1 value of the normal myocardial tissue (1100 ms). (b) T1 recovery curves for on-resonance (0 Hz) and off-resonance (100 Hz) spins, and estimated ($\widehat{T1}$) values.

Figure 4.9 (a) shows the magnetization of the MOLLI images as a function of the off-resonance frequencies for a simulated T1 value of the normal myocardial tissue (1100 ms). Figure 4.9 (b) depicts the T1 recovery curves for on-resonance (0 Hz) and off-resonance

(100 Hz) spins. The different level of magnetization influenced the estimated T1 after model fitting ($\widehat{T1}$).

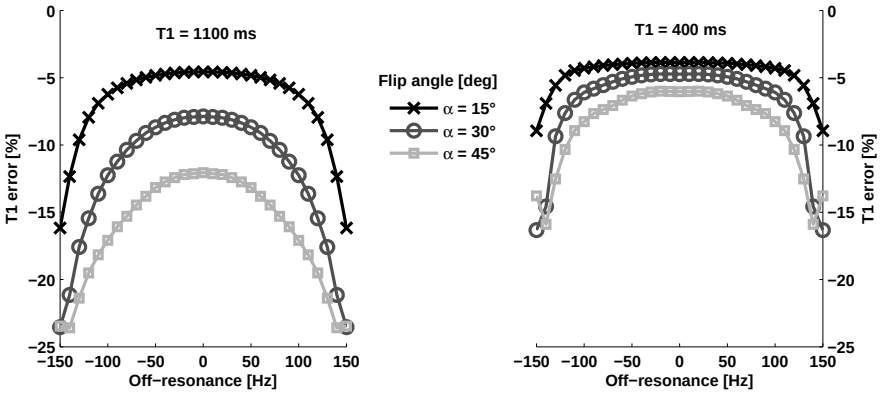


Figure 4.10: Influence of the flip angle on T1 underestimation due to off-resonance effects for simulated T1 values typical of myocardial tissue before (left panel) and after (right panel) gadolinum contrast agent administration.

T1 underestimation due to off-resonance effects was also found to be influenced by the flip angle choice, as shown in Figure 4.10. Sensitivity to off-resonance increased for larger flip angles and for higher T1 values. In addition, the choice of the repetition time (TR) of the SSFP readout affected the sensitivity to off-resonance as demonstrated by the simulation results shown in Figure 4.11.

### 4.4.2 In-vivo results

The MOLLI pulse sequence was implemented on 3T Philips Ingenia system (Philips Healthcare, Best, the Netherlands). A short-axis slice was acquired using the following parameters: field of view

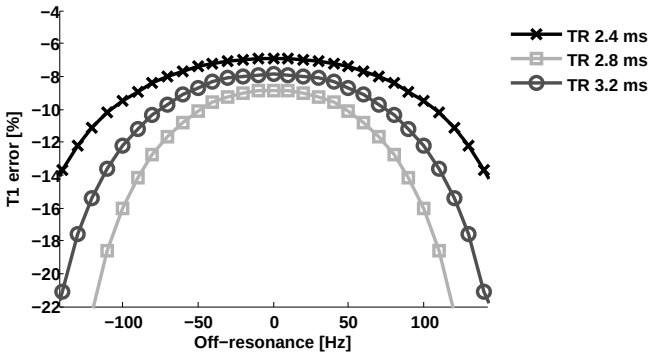


Figure 4.11: Influence of the repetition time (TR) of the SSFP readout in the T1 underestimation due to off-resonance effects.

(FOV) 350 × 300 mm, slice thickness 10 mm, in-plane resolution 1.8 × 2.1 mm, flip angle 30°, TR/TE 2.4/1.2 ms, SENSE factor 2 and partial Fourier acquisition. The inversion time (TI) of the first MOLLI images of the three LL experiments were 100, 200 and 350 ms, respectively (see Fig. 4.2. The effective inversion time of the other images was calculated using the Eq. 4.1 where the R-R interval was estimated from the metadata of the DICOM file of each image. Pixel-wise T1 mapping was performed by data fitting with the three-parameter model of Eq. 4.2 was performed using a custom written Matlab (The Mathworks, Natick, MA, USA) software.

Figure 4.12 shows an example of the eleven MOLLI images acquired on a healthy volunteer. Spatial co-registration between images allows to perform pixel-wise T1 mapping. Figure 4.13 depicts the polar map of the mean T1 values after the segmentation of the T1 map in six myocardial regions according to short-axis model of the mid-cavity of the American Heart Association [74].

The mean T1 value across segments of $1082.6 \pm 22.7$ ms (Tab.4.1)

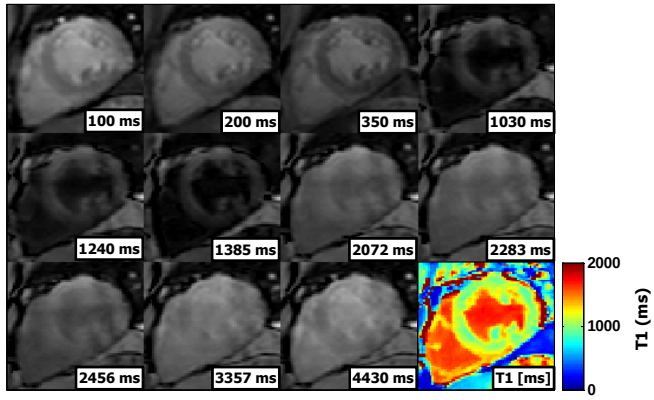


Figure 4.12: MOLLI T1 mapping in healthy volunteer.

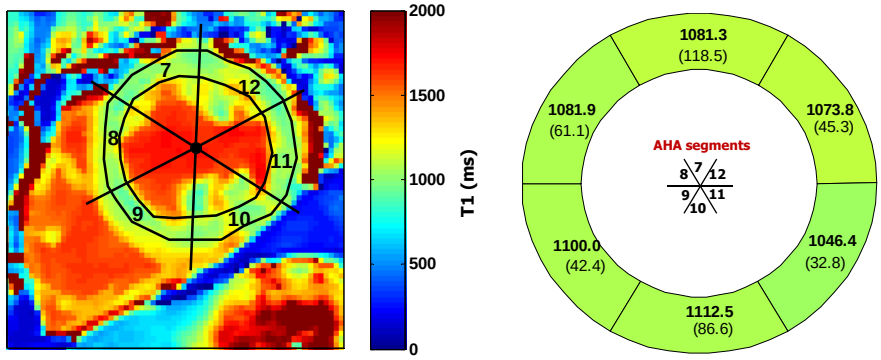


Figure 4.13: T1 mapping in a healthy volunteer using the implemented MOLLI sequence.

Table 4.1: T1 values in six myocardial segments (Mean ± standard deviation) obtained in a healthy volunteer.

| N° | Segment | T1 value [ms] |
|---|---|---|
| 7 | anterior | 1081.3 ± 118.5 |
| 8 | anteroseptal | 1081.9 ± 61.1 |
| 9 | inferoseptal | 1100.0 ± 42.4 |
| 10 | inferior | 1112.5 ± 86.6 |
| 11 | inferolateral | 1046.4 ± 32.8 |
| 12 | anterolateral | 1073.8 ± 45.3 |
| | Mean over segments | 1082.6 ± 22.7 |

is in good agreement with T1 values reported recently at 3T [73].

Figure 4.14 (a) shows the T1 map obtained in a patient with acute myocardial infarction in the anteroseptal region. T1 value in a ROI in this region (1483 ± 32 ms) was significantly higher than in a ROI in the inferoseptal region (1263 ± 56 ms). T1 underestimation in the lateral wall, indicated by red arrows in Fig. 4.14, was found to be correlated to large B0-field inhomogeneities as depicted in Fig. 4.14 (b). B0-field map was calculated as in [64] from phase images acquired using a dual-echo gradient echo sequence.

## 4.5 Discussion

In this study a MOLLI pulse sequence for myocardial T1 mapping has been implemented on a 3.0 T MRI system. A Bloch's equation simulator has been developed to investigate the influence of pulse

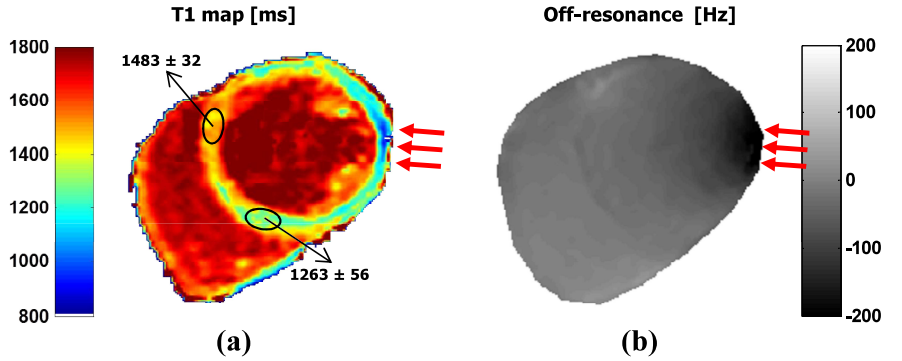


Figure 4.14: (a) T1 map in a patient with myocardial infarction in the anteroseptal region. (b) Field map calculated from phase images acquired using a dual-echo gradient echo sequence.

sequence parameters on T1 estimation. Simulation results showed a complex dependence of the estimated T1 on scan parameters (flip angle, TR), tissue relaxation times (T1,T2) and acquisition conditions (heart rate, B0-field inhomogeneity).

The use of minimum delay of six seconds between inversion pulses, instead of a resting period of three heartbeats between LL experiments as in the original version of MOLLI [17], was demonstrated to be a useful strategy to reduce the dependence of the heart rate on T1 estimation, as shown in Fig. 4.6.

The perturbation of the longitudinal recovery due to the SSFP readouts used for MOLLI image acquisition was shown to cause systematic T1 underestimation. Simulation results showed that this negative bias is increased for larger flip angles, for tissues with shorter T2 and longer T1.

The presence of B0-inhomogeneities was demonstrated to cause a further T1 underestimation which depends on off-resonance values.

Thus, B0-inhomogeneities can result in artifactual regional variation of T1. In addition, sensitivity to off-resonance was found to increase for larger flip angles, longer repetition times (TR) and for higher T1 values.

*In-vivo* results showed that the implemented pulse sequence allowed the acquisition of images with different effective inversion times in a single breath-hold. This ensured the spatial co-registration between images, a fundamental prerequisite for performing pixel-wise T1 mapping. T1 mapping obtained in a healthy volunteer showed T1 values (mean value 1082 ms) in good agreement with previous literature at 3.0 T [73], with low standard deviation across myocardial segments (SD = 22.7 ms). In a patient with acute myocardial infarction, the T1 was found higher (of about 200 ms) in the infarcted than in a remote area, coherently with values previously reported at 1.5 [66]. However, B0-inhomogeneity was shown to produce an artefactual regional variation of the estimated T1, as anticipated by the simulation results on off-resonance effects. Since 3.0 Tesla MRI systems often encountered B0-inhomogeneity issues, future efforts will be focused on the development of strategies for compensation of the T1 underestimation by exploiting the simulation results and B0-field maps acquired *in-vivo*.

# Chapter 5

# Conclusions

Magnetic Resonance Imaging (MRI) and Spectroscopy (MRS) techniques can provide fundamental information for tissue characterization in normal and diseased myocardium. Cardiac MRS allows the quantification of crucial compounds involved in myocardial energy metabolism, such as triglycerides (TGs) and creatine (CR). On the other hand, quantitative MRI methods, as T1 mapping, can give insights into different physiopathological conditions (inflammation, edema, fibrosis) of myocardial tissue. However, several methodological challenges have limited the reproducibility of the studies and the application of these techniques in clinical settings.

The PhD project focused on the development of new methods in Cardiac Magnetic Resonance Imaging and Spectroscopy for the noninvasive myocardial tissue characterization *in vivo*.

In the first part of the thesis (Chapter 2) the problem of the optimal reconstruction of multichannel cardiac MRS data has been investigated. Different coil combination strategies have been imple-

mented: SNR weighting, PCA combination and image-based combination. Simulations on synthetic datasets have been carried out to evaluate the SNR performance of the different coil combination algorithms.

Respiratory compensation strategies have been implemented both in the acquisition stage and in the post–processing of the acquired spectra. In particular, the respiratory navigator (RNAV) technique was integrated in a point-resoveld spectroscopy (PRESS) sequence for single-voxel $^{1}$H-MRS.

The feasibility of $^{1}$H cardiac spectroscopy using two coil arrays with 5 and 32 elements has been demonstrated in a volunteer study. The spectral quality allowed for the estimation of TG and CR contents with values in good agreement with previous literature and a high correlation between the quantification results obtained by the two coil arrays. All coil combination strategies showed comparable SNR values and quality in the resulting spectra. On average, the mean SNR of the 32-element array was about 24% higher than that of the 5-element coil. In addition to an advantage in SNR performance, large coil arrays also provide sufficient coverage, rendering coil repositioning during examinations unnecessary.

Since large coil arrays are today widespread in cardiovascular MRI, these results will contribute towards the integration of cardiac proton spectroscopy into clinical protocols.

The second part of the thesis (Chapter 3) focused on the implementation of a fast spectroscopic imaging method able to provide regional distribution of cardiac metabolites.

To this end, an optimized Echo-Planar Spectroscopic Imaging

(EPSI) technique was developed. Respiratory navigator gating and ECG triggering were integrated in the EPSI sequence for respiratory and cardiac motion compensation, respectively.

A suitable software package was developed for the reconstruction of EPSI data, with water unsuppressed data used for coil complex sensitivity maps estimation, spectral Nyquist ghost artifact removal and static field inhomogeneity (B0) correction. In addition a Bloch's equations simulator was developed in order to explore the influence of cardiac motion on signal encoding in the readout direction of the EPSI sequence.

Experiments were carried on healthy volunteers to validate the EPSI technique *in vivo*. For comparison single voxel $^{1}$H-MRS measurements were performed with a PRESS sequence in a volume in the interventricular septum. Results showed that the spectral quality of the EPSI was found to be comparable to the PRESS in the septum. The small spectral linewidths allowed a good discrimination of the resonances of trimethyl ammonium (TMA) at 3.2 ppm and CR at 3.01 ppm. Concerning quantification, a high correlation between EPSI and PRESS was found in the estimated concentration of TG and CR in the septum. A lower correlation was found in other myocardial segments, in particular close to the posterior vein of the left ventricle. EPSI spectra from these regions were characterized by increased linewidths associated to B0 inhomogeneities.

In summary, the EPSI technique was demonstrated to be a valuable tool for the assessment of the spatial distributions of myocardial TG and CR content.

The last part of the thesis (Chapter 4) focused on the develop-

ment of a quantitative MRI technique for myocardial T1 quantification based on MOLLI pulse sequence.

The influence of pulse sequence parameters on T1 estimation has been investigated through numerical simulations of Bloch's equations. Simulation results showed a complex dependence of the estimated T1 on scan parameters (flip angle, TR), tissue relaxation times (T1,T2) and acquisition conditions (heart rate, B0-field inhomogeneity). The use of minimum delay of six seconds between inversion pulses reduced the dependency to heart rate on T1 estimation compared to the original version of MOLLI which used a resting period of three heartbeats between Look-Locker experiments.

Simulation results also showed that the perturbation of the longitudinal recovery due to SSFP readouts leads to a systematic T1 underestimation, and this negative bias increases for larger flip angles and for tissues with shorter T2 and longer T1. Also, off-resonance effects due to B0-inhomogeneities was shown to be a reason of further T1 underestimation that increases for larger flip angles, longer repetition times (TR) and for higher T1 values.

*In-vivo* results showed that the implemented pulse sequence allowed the acquisition of images with different effective inversion times in a single breath-hold. This ensured the spatial co-registration between images, a fundamental prerequisite for performing pixel-wise T1 mapping. T1 values obtained in healthy myocardium were consistent with previous studies at 3.0 Tesla, with reasonable low variations across myocardial segments. The T1 value measured in the infarcted myocardium was found to be significantly higher, in good agreement with values previously reported in literature. However, as anticipated by the simulation results, B0 inhomogeneities

across myocardium led to an artefactual regional variation of T1. Given the fact that 3.0 Tesla MRI systems often suffer from B0-inhomogeneity issues, future work on this T1 mapping method will be focused on the reduction of the sensitivity to off-resonance effects and on the development of strategies for the compensation of T1 underestimation, such as by incorporating the simulation results and B0-field maps acquired *in-vivo*.

In this thesis, a variety of methods have been presented to address some of the current limitations of cardiac MRI and MRS concerning low SNR, motion sensitivity, long scan times and reproducibility issues. The results achieved by the proposed methods may facilitate the use of MRI and MRS in clinical settings for myocardial tissue characterization.

# Appendix A

# List of Abbreviations and Symbols

| | |
|---|---|
| **AHA** | **A**merican **H**eart **A**ssociation |
| **AMARES** | **A**dvanced **M**ethod **f**or Accurate, **R**obust and **E**fficient **S**pectral fitting |
| **B0** | Static magnetic field |
| **B1** | Radio-frequency magnetic field |
| **CR** | **CR**eatine |
| **EPSI** | **E**cho **P**lanar **S**pectroscopic **I**maging |
| **FID** | **F**ree **I**nduction **D**ecay |
| **FOV** | **F**ield **O**f **V**iew |
| **FOX** | **F**ield **O**f E**X**citation |
| **GBCA** | **G**adolinium-**b**ased **C**ontrast **A**gents |
| **IR** | **I**nversion **R**ecovery |
| **LFA** | **L**inear **F**lip **A**ngle |
| **LGE** | **L**ate **G**adolinium **E**nhancement |

| | |
|---|---|
| **MOLLI** | **MO**dified **L**ook-**L**ocker **I**nversion recovery |
| **MRI** | **M**agnetic **R**esonance **I**maging |
| **MRS** | **M**agnetic **R**esonance **S**pectroscopy |
| **PCA** | **P**rincipal **C**omponent **A**nalysis |
| **PRESS** | **P**oint-**RES**olved **S**pectroscopy |
| **RF** | **R**adio **F**requency |
| **RNAV** | **R**espiratory **N**avigator |
| **ROI** | **R**egion **o**f **I**nterest |
| **SNR** | **S**ignal-to-**N**oise **R**atio |
| **SSFP** | **S**teady **S**tate **F**ree **P**recession |
| **SV** | **S**ingle **V**oxel |
| **T1** | Longitudinal relaxation time |
| **T2** | Transverse relaxation time |
| **TE** | **E**cho **T**ime |
| **TG** | **T**rig**l**ycerides |
| **TI** | **I**nversion **T**ime |
| **TMA** | **T**rimethyl **A**mmonium |
| **TR** | **R**epetition **T**ime |

# Appendix B

# Authored and co-authored publications

## Publications in peer-reviewed journals

K. Weiss, **N. Martini**, P. Boesiger, S. Kozerke. "Cardiac proton spectroscopy using large coil arrays", *NMR Biomed.* 2013 Mar; 26(3): 276-84.

K. Weiss, **N. Martini**, P. Boesiger, S. Kozerke. "Metabolic MR imaging of regional triglyceride and creatine content in the human heart". *Magn Reson Med.* 2012 Dec; 68(6): 1696-704.

G. Giovannetti, **N. Martini**, N. Di Lascio, N. Vanello, V. Positano, V. Hartwig, D. De Marchi , L. Lombardi, L. Landini, M.F. Santarelli. "Filter design for phased-array MR image reconstruction using super algorithm", *Concepts in Magnetic Resonance Part B*

2012 Aug;41B(3), 85-93.

**N. Martini**, D. Menicucci, L. Sebastiani, R. Bedini, A. Pingitore, N. Vanello, M. Milanesi, L. Landini, A. Gemignani. "The dynamics of EEG gamma responses to unpleasant visual stimuli: from local activity to functional connectivity". *Neuroimage* 2012 Apr 2;60(2):922-32.

## Publications in international conferences

**N. Martini**, K. Weiss, P. Boesiger, D. Chiappino and S. Kozerke, "Multi-channel Proton Spectroscopy of the Heart", *Proceedings of the 19th Annual Meeting ISMRM*, Montréal-Québec, Canada, 2011:1359.

K. Weiss, **N. Martini**, P. Boesiger, and S. Kozerke, "Two-dimensional mapping of triglyceride and creatine content of the human heart", *Proceedings of the 19th Annual Meeting ISMRM*, Montréal–Québec, Canada, 2011:619.

K. Weiss, **N. Martini**, P. Boesiger, and S. Kozerke, "Three–Dimensional Local–Look Spectroscopic Imaging of the Heart", *Proceedings of the 19th Annual Meeting ISMRM*, Montréal–Québec, Canada 2011:620.

K. Weiss, **N. Martini**, P. Boesiger, and S. Kozerke, "Local-look navigator gated and cardiac triggered echo-planar spectroscopic imaging of the heart", *J Cardiovasc Magn Reson.* 2011; 13(Suppl 1): O78.

# Bibliography

[1] L. S. Szczepaniak, R. L. Dobbins, G. J. Metzger, G. Sartoni-D'Ambrosia, D. Arbique, W. Vongpatanasin, R. Unger, and R. G. Victor, "Myocardial triglycerides and systolic function in humans: in vivo evaluation by localized proton spectroscopy and cardiac imaging.," *Magn Reson Med*, vol. 49, pp. 417–423, Mar 2003.

[2] L. J. Rijzewijk, R. W. van der Meer, J. W. A. Smit, M. Diamant, J. J. Bax, S. Hammer, J. A. Romijn, A. de Roos, and H. J. Lamb, "Myocardial steatosis is an independent predictor of diastolic dysfunction in type 2 diabetes mellitus.," *J Am Coll Cardiol*, vol. 52, pp. 1793–1799, Nov 2008.

[3] P. A. Bottomley and R. G. Weiss, "Non-invasive magnetic-resonance detection of creatine depletion in non-viable infarcted myocardium," *The Lancet*, vol. 351, no. 9104, pp. 714–718, 1998.

[4] A. Haase, J. Frahm, W. Hnicke, and D. Matthaei, "$^{1}$H NMR chemical shift selective (CHESS) imaging.," *Phys Med Biol*, vol. 30, pp. 341–344, Apr 1985.

[5] A. Coron, L. Vanhamme, J. P. Antoine, P. V. Hecke, and S. V. Huffel, "The filtering approach to solvent peak suppression in MRS: a critical review.," *J Magn Reson*, vol. 152, pp. 26–40, Sep 2001.

[6] R. W. van der Meer, J. Doornbos, S. Kozerke, M. Schr, J. J. Bax, S. Hammer, J. W. A. Smit, J. A. Romijn, M. Diamant, L. J. Rijzewijk, A. de Roos, and H. J. Lamb, "Metabolic imaging of myocardial triglyceride content: reproducibility of $^{1}$H MR spectroscopy with respiratory navigator gating in volunteers.," *Radiology*, vol. 245, pp. 251–257, Oct 2007.

[7] J. M. McGavock, I. Lingvay, I. Zib, T. Tillery, N. Salas, R. Unger, B. D. Levine, P. Raskin, R. G. Victor, and L. S. Szczepaniak, "Cardiac steatosis in diabetes mellitus: a $^{1}$H-magnetic resonance spectroscopy study.," *Circulation*, vol. 116, pp. 1170–1175, Sep 2007.

[8] R. Pohmann, M. von Kienlin, and A. Haase, "Theoretical evaluation and comparison of fast chemical shift imaging methods.," *J Magn Reson*, vol. 129, pp. 145–160, Dec 1997.

[9] R. De Graaf, "Single volume localization and water suppression.," *In: In vivo NMR spectroscopy: principles and techniques, 2nd edn. Wiley, Chichester.*, pp. 349–387, 2007.

[10] S. Posse, G. Tedeschi, R. Risinger, R. Ogg, and D. Le Bihan, "High speed $^{1}$H spectroscopic imaging in human brain by echo planar spatial-spectral encoding.," *Magn Reson Med*, vol. 33, pp. 34–40, Jan 1995.

[11] M. L. Zierhut, E. Ozturk-Isik, A. P. Chen, I. Park, D. B. Vigneron, and S. J. Nelson, "1H spectroscopic imaging of human brain at 3 Tesla: comparison of fast three-dimensional magnetic resonance spectroscopic imaging techniques.," *J Magn Reson Imaging*, vol. 30, pp. 473–480, Sep 2009.

[12] M. A. Thomas, R. Nagarajan, A. Huda, D. Margolis, M. K. Sarma, K. Sheng, R. E. Reiter, and S. S. Raman, "Multidimensional MR spectroscopic imaging of prostate cancer in vivo.," *NMR Biomed*, vol. 27, pp. 53–66, Jan 2014.

[13] C. J. Holloway, N. Ntusi, J. Suttie, M. Mahmod, E. Wainwright, G. Clutton, G. Hancock, P. Beak, A. Tajar, S. K. Piechnik, J. E. Schneider, B. Angus, K. Clarke, L. Dorrell, and S. Neubauer, "Comprehensive cardiac magnetic resonance imaging and spectroscopy reveal a high burden of myocardial disease in HIV patients.," *Circulation*, vol. 128, pp. 814–822, Aug 2013.

[14] S. Dass, J. J. Suttie, S. K. Piechnik, V. M. Ferreira, C. J. Holloway, R. Banerjee, M. Mahmod, L. Cochlin, T. D. Karamitsos, M. D. Robson, H. Watkins, and S. Neubauer, "Myocardial tissue characterization using magnetic resonance noncontrast t1 mapping in hypertrophic and dilated cardiomyopathy.," *Circ Cardiovasc Imaging*, vol. 5, pp. 726–733, Nov 2012.

[15] G. J. Stanisz, E. E. Odrobina, J. Pun, M. Escaravage, S. J. Graham, M. J. Bronskill, and R. M. Henkelman, "T1, T2 relaxation and magnetization transfer in tissue at 3T.," *Magn Reson Med*, vol. 54, pp. 507–512, Sep 2005.

[16] S. J. Flacke, S. E. Fischer, and C. H. Lorenz, "Measurement of the gadopentetate dimeglumine partition coefficient in human myocardium in vivo: normal distribution and elevation in acute and chronic infarction.," *Radiology*, vol. 218, pp. 703–710, Mar 2001.

[17] D. R. Messroghli, A. Radjenovic, S. Kozerke, D. M. Higgins, M. U. Sivananthan, and J. P. Ridgway, "Modified look-locker inversion recovery (MOLLI) for high-resolution t1 mapping of the heart.," *Magn Reson Med*, vol. 52, pp. 141–146, Jul 2004.

[18] S. K. Piechnik, V. M. Ferreira, E. Dall'Armellina, L. E. Cochlin, A. Greiser, S. Neubauer, and M. D. Robson, "Shortened modified look-locker inversion recovery (ShMOLLI) for clinical myocardial T1-mapping at 1.5 and 3 T within a 9 heartbeat breathhold.," *J Cardiovasc Magn Reson*, vol. 12, p. 69, 2010.

[19] K. Chow, J. A. Flewitt, J. D. Green, J. J. Pagano, M. G. Friedrich, and R. B. Thompson, "Saturation recovery single-shot acquisition (SASHA) for myocardial T1 mapping.," *Magn Reson Med*, Jul 2013.

[20] K. Weiss, N. Martini, P. Boesiger, and S. Kozerke, "Cardiac proton spectroscopy using large coil arrays.," *NMR Biomed*, vol. 26, pp. 276–284, Mar 2013.

[21] M. Horn, "Cardiac magnetic resonance spectroscopy: a window for studying physiology.," *Methods Mol Med*, vol. 124, pp. 225–248, 2006.

[22] L. E. Hudsmith and S. Neubauer, "Magnetic resonance spectroscopy in myocardial disease.," *JACC Cardiovasc Imaging*, vol. 2, pp. 87–96, Jan 2009.

[23] I. Nakae, K. Mitsunami, T. Omura, T. Yabe, T. Tsutamoto, S. Matsuo, M. Takahashi, S. Morikawa, T. Inubushi, Y. Nakamura, M. Kinoshita, and M. Horie, "Proton magnetic resonance spectroscopy can detect creatine depletion associated with the progression of heart failure in cardiomyopathy.," *J Am Coll Cardiol*, vol. 42, pp. 1587–1593, Nov 2003.

[24] J. Felblinger, B. Jung, J. Slotboom, C. Boesch, and R. Kreis, "Methods and reproducibility of cardiac/respiratory double-triggered $^{1}$H-MR spectroscopy of the human heart.," *Magn Reson Med*, vol. 42, pp. 903–910, Nov 1999.

[25] M. Kankaanpää, H.-R. Lehto, J. P. Pärkkä, M. Komu, A. Viljanen, E. Ferrannini, J. Knuuti, P. Nuutila, R. Parkkola, and P. Iozzo, "Myocardial triglyceride content and epicardial fat mass in human obesity: relationship to left ventricular function and serum free fatty acid levels," *Journal of Clinical Endocrinology & Metabolism*, vol. 91, no. 11, pp. 4689–4695, 2006.

[26] B. Rial, M. D. Robson, S. Neubauer, and J. E. Schneider, "Rapid quantification of myocardial lipid content in humans using single breath-hold $^{1}$H MRS at 3 Tesla," *Magnetic Resonance in Medicine*, vol. 66, no. 3, pp. 619–624, 2011.

[27] S. Kozerke, M. Schär, H. J. Lamb, and P. Boesiger, "Volume tracking cardiac $^{31}$P spectroscopy," *Magnetic resonance in medicine*, vol. 48, no. 2, pp. 380–384, 2002.

[28] M. Schär, S. Kozerke, and P. Boesiger, "Navigator gating and volume tracking for double-triggered cardiac proton spectroscopy at 3 Tesla.," *Magn Reson Med*, vol. 51, pp. 1091–1095, Jun 2004.

[29] B. J. Wintersperger, S. B. Reeder, K. Nikolaou, O. Dietrich, A. Huber, A. Greiser, T. Lanz, M. F. Reiser, and S. O. Schoenberg, "Cardiac CINE MR imaging with a 32-channel cardiac coil and parallel imaging: impact of acceleration factors on image quality and volumetric accuracy.," *J Magn Reson Imaging*, vol. 23, pp. 222–227, Feb 2006.

[30] K. Nehrke, P. Brnert, P. Mazurkewitz, R. Winkelmann, and I. Grsslin, "Free-breathing whole-heart coronary MR angiography on a clinical scanner in four minutes.," *J Magn Reson Imaging*, vol. 23, pp. 752–756, May 2006.

[31] P. B. Roemer, W. A. Edelstein, C. E. Hayes, S. P. Souza, and O. M. Mueller, "The NMR phased array.," *Magn Reson Med*, vol. 16, pp. 192–225, Nov 1990.

[32] K. P. Pruessmann, M. Weiger, M. B. Scheidegger, and P. Boesiger, "SENSE: sensitivity encoding for fast MRI.," *Magn Reson Med*, vol. 42, pp. 952–962, Nov 1999.

[33] N. Martini, M. F. Santarelli, G. Giovannetti, M. Milanesi, D. D. Marchi, V. Positano, and L. Landini, "Noise correlations and

SNR in phased-array MRS.," *NMR Biomed*, vol. 23, pp. 66–73, Jan 2010.

[34] S. M. Wright and L. L. Wald, "Theory and application of array coils in MR spectroscopy.," *NMR Biomed*, vol. 10, pp. 394–410, Dec 1997.

[35] M. Bydder, G. Hamilton, T. Yokoo, and C. B. Sirlin, "Optimal phased-array combination for spectroscopy.," *Magn Reson Imaging*, vol. 26, pp. 847–850, Jul 2008.

[36] C. T. Rodgers and M. D. Robson, "Receive array magnetic resonance spectroscopy: Whitened singular value decomposition WSVD gives optimal bayesian solution.," *Magn Reson Med*, vol. 63, pp. 881–891, Apr 2010.

[37] M. Buehrer, K. P. Pruessmann, P. Boesiger, and S. Kozerke, "Array compression for MRI with large coil arrays.," *Magn Reson Med*, vol. 57, pp. 1131–1139, Jun 2007.

[38] E. D. Becker, J. A. Ferretti, and P. N. Gambhir, "Selection of optimum parameters for pulse Fourier transform nuclear magnetic resonance," *Analytical Chemistry*, vol. 51, no. 9, pp. 1413–1420, 1979.

[39] R. E. Gabr, S. Sathyanarayana, M. Schr, R. G. Weiss, and P. A. Bottomley, "On restoring motion-induced signal loss in single-voxel magnetic resonance spectra.," *Magn Reson Med*, vol. 56, pp. 754–760, Oct 2006.

[40] P. A. Bottomley, "Spatial localization in NMR spectroscopy in vivo.," *Ann N Y Acad Sci*, vol. 508, pp. 333–348, 1987.

[41] A. Naressi, C. Couturier, J. M. Devos, M. Janssen, C. Mangeat, R. de Beer, and D. Graveron-Demilly, "Java-based graphical user interface for the MRUI quantitation package.," *MAGMA*, vol. 12, pp. 141–152, May 2001.

[42] H. Bongers, F. Schick, M. Skalej, W. I. Jung, and A. Stevens, "Localized in vivo $^{1}$H spectroscopy of human skeletal muscle: normal and pathologic findings.," *Magn Reson Imaging*, vol. 10, no. 6, pp. 957–964, 1992.

[43] F. Schick, B. Eismann, W.-I. Jung, H. Bongers, M. Bunse, and O. Lutz, "Comparison of localized proton NMR signals of skeletal muscle and fat tissue in vivo: two lipid compartments in muscle tissue," *Magnetic resonance in medicine*, vol. 29, no. 2, pp. 158–167, 1993.

[44] L. S. Szczepaniak, E. E. Babcock, F. Schick, R. L. Dobbins, A. Garg, D. K. Burns, J. D. McGarry, and D. T. Stein, "Measurement of intracellular triglyceride stores by $^{1}$H spectroscopy: validation in vivo," *American Journal of Physiology-Endocrinology And Metabolism*, vol. 276, no. 5, pp. E977–E989, 1999.

[45] L. Barantin, A. Le Pape, and S. Akoka, "A new method for absolute quantitation of MRS metabolites.," *Magn Reson Med*, vol. 38, pp. 179–182, Aug 1997.

[46] K. Weiss, S. Summermatter, C. T. Stoeck, and S. Kozerke, "Compensation of signal loss due to cardiac motion in point-resolved spectroscopy of the heart.," *Magn Reson Med*, Nov 2013.

[47] K. Weiss, N. Martini, P. Boesiger, and S. Kozerke, "Metabolic MR imaging of regional triglyceride and creatine content in the human heart.," *Magn Reson Med*, vol. 68, pp. 1696–1704, Dec 2012.

[48] J. A. den Hollander, W. T. Evanochko, and G. M. Pohost, "Observation of cardiac lipids in humans by localized $^{1}$H magnetic resonance spectroscopic imaging.," *Magn Reson Med*, vol. 32, pp. 175–180, Aug 1994.

[49] R. D. O'Connor, J. Xu, G. A. Ewald, J. J. H. Ackerman, L. R. Peterson, R. J. Gropler, and A. Bashir, "Intramyocardial triglyceride quantification by magnetic resonance spectroscopy: In vivo and ex vivo correlation in human subjects.," *Magn Reson Med*, vol. 65, pp. 1234–1238, May 2011.

[50] W. C. Stanley, F. A. Recchia, and G. D. Lopaschuk, "Myocardial substrate metabolism in the normal and failing heart.," *Physiol Rev*, vol. 85, pp. 1093–1129, Jul 2005.

[51] S. Neubauer, "The failing heart–an engine out of fuel.," *N Engl J Med*, vol. 356, pp. 1140–1151, Mar 2007.

[52] P. A. Bottomley and R. G. Weiss, "Noninvasive localized MR quantification of creatine kinase metabolites in normal and in-

farcted canine myocardium.," *Radiology*, vol. 219, pp. 411–418, May 2001.

[53] H. P. Hetherington, D. J. Luney, J. T. Vaughan, J. W. Pan, S. L. Ponder, O. Tschendel, D. B. Twieg, and G. M. Pohost, "3D $^{31}$P spectroscopic imaging of the human heart at 4.1 T.," *Magn Reson Med*, vol. 33, pp. 427–431, Mar 1995.

[54] J.-P. Heyne, R. Rzanny, A. Hansch, U. Leder, J. R. Reichenbach, and W. A. Kaiser, "3D $^{31}$P-MR spectroscopic imaging in hypertensive heart disease.," *Eur Radiol*, vol. 16, pp. 1796–1802, Aug 2006.

[55] R. Pohmann and M. von Kienlin, "Accurate phosphorus metabolite images of the human heart by 3D acquisition-weighted CSI.," *Magn Reson Med*, vol. 45, pp. 817–826, May 2001.

[56] P. Mansfield, "Spatial mapping of the chemical shift in NMR.," *Magn Reson Med*, vol. 1, pp. 370–386, Sep 1984.

[57] W. Du, Y. P. Du, X. Fan, M. A. Zamora, and G. S. Karczmar, "Reduction of spectral ghost artifacts in high-resolution echo-planar spectroscopic imaging of water and fat resonances.," *Magn Reson Med*, vol. 49, pp. 1113–1120, Jun 2003.

[58] F. Harris, "On the use of windows for harmonic analysis with the discrete Fourier transform," *Proc. IEEE*, vol. 66, no. 1, pp. 51–83, 1978.

[59] Vanhamme, van den Boogaart A, and Van Huffel S, "Improved method for accurate and efficient quantification of MRS data with use of prior knowledge," *J Magn Reson*, vol. 129, pp. 35–43, Nov 1997.

[60] W. Pijnappel, A. Van den Boogaart, R. De Beer, and D. Van Ormondt, "SVD-based quantification of magnetic resonance signals," *Journal of Magnetic Resonance*, vol. 97, no. 1, pp. 122–134, 1992.

[61] U. Gamper, P. Boesiger, and S. Kozerke, "Diffusion imaging of the in vivo heart using spin echoes–considerations on bulk motion sensitivity.," *Magn Reson Med*, vol. 57, pp. 331–337, Feb 2007.

[62] G. H. Mangun and V. C. Myers, "Normal creatine, phosphorus, and potassium content of human cardiac and voluntary muscle," *J. Biol. Chem.*, vol. 135, pp. 411–414, 1940.

[63] L. Nascimben, J. S. Ingwall, P. Pauletto, J. Friedrich, J. K. Gwathmey, V. Saks, A. C. Pessina, and P. D. Allen, "Creatine kinase system in failing and nonfailing human myocardium.," *Circulation*, vol. 94, pp. 1894–1901, Oct 1996.

[64] S. B. Reeder, A. Z. Faranesh, J. L. Boxerman, and E. R. McVeigh, "In vivo measurement of $T2^*$ and field inhomogeneity maps in the human heart at 1.5 T.," *Magn Reson Med*, vol. 39, pp. 988–998, Jun 1998.

[65] N. Mewton, C. Y. Liu, P. Croisille, D. Bluemke, and J. A. Lima, "Assessment of myocardial fibrosis with cardiovascular

magnetic resonance," *Journal of the American College of Cardiology*, vol. 57, no. 8, pp. 891–903, 2011.

[66] D. R. Messroghli, K. Walters, S. Plein, P. Sparrow, M. G. Friedrich, J. P. Ridgway, and M. U. Sivananthan, "Myocardial T1 mapping: application to patients with acute and chronic myocardial infarction.," *Magn Reson Med*, vol. 58, pp. 34–40, Jul 2007.

[67] J. C. Moon, D. R. Messroghli, P. Kellman, S. K. Piechnik, M. D. Robson, M. Ugander, P. D. Gatehouse, A. E. Arai, M. G. Friedrich, S. Neubauer, J. Schulz-Menger, and E. B. Schelbert, "Myocardial T1 mapping and extracellular volume quantification: a society for cardiovascular magnetic resonance (SCMR) and CMR Working Group of the European Society of Cardiology consensus statement.," *J Cardiovasc Magn Reson*, vol. 15, p. 92, Oct 2013.

[68] M. Milanesi, A. Barison, V. Positano, P. G. Masci, D. De Marchi, L. Marinelli, C. J. Hardy, T. K. Foo, L. Landini, and M. Lombardi, "Modified cine inversion recovery pulse sequence for the quantification of myocardial T1 and gadolinium partition coefficient.," *J Magn Reson Imaging*, vol. 37, pp. 109–118, Jan 2013.

[69] K. Scheffler and S. Lehnhardt, "Principles and applications of balanced SSFP techniques.," *Eur Radiol*, vol. 13, pp. 2409–2418, Nov 2003.

[70] S. Nekolla, T. Gneiting, J. Syha, R. Deichmann, and A. Haase, "T1 maps by K-space reduced snapshot-FLASH MRI.," *J Comput Assist Tomogr*, vol. 16, no. 2, pp. 327–332, 1992.

[71] B. A. Hargreaves, S. S. Vasanawala, J. M. Pauly, and D. G. Nishimura, "Characterization and reduction of the transient response in steady-state MR imaging.," *Magn Reson Med*, vol. 46, pp. 149–158, Jul 2001.

[72] V. S. Deshpande, Y.-C. Chung, Q. Zhang, S. M. Shea, and D. Li, "Reduction of transient signal oscillations in true-FISP using a linear flip angle series magnetization preparation.," *Magn Reson Med*, vol. 49, pp. 151–157, Jan 2003.

[73] F. von Knobelsdorff-Brenkenhoff, M. Prothmann, M. A. Dieringer, R. Wassmuth, A. Greiser, C. Schwenke, T. Niendorf, and J. Schulz-Menger, "Myocardial T1 and T2 mapping at 3 T: reference values, influencing factors and implications.," *J Cardiovasc Magn Reson*, vol. 15, p. 53, Jun 2013.

[74] M. D. Cerqueira, N. J. Weissman, V. Dilsizian, A. K. Jacobs, S. Kaul, W. K. Laskey, D. J. Pennell, J. A. Rumberger, T. Ryan, M. S. Verani, A. H. A. W. G. o. M. S. , and R. for Cardiac Imaging, "Standardized myocardial segmentation and nomenclature for tomographic imaging of the heart. a statement for healthcare professionals from the cardiac imaging committee of the council on clinical cardiology of the american heart association.," *Circulation*, vol. 105, pp. 539–542, Jan 2002.